Chapter 3
Progress in Short-Pulse Yb-Doped Fiber Oscillators and Amplifiers

**Ci-Ling Pan, Alexey Zaytsev, Chih-Hsuan Lin and Yi-Jing You**

3.1 Introduction

Recently, high-speed and high-power fiber lasers have emerged not only as a workhorse for information technology but also as a viable alternative to current generation of main-frame lasers for industrial and scientific applications [1, 2]. Laser machining and processing of materials, e.g., welding, drilling and precision cutting, are among the most important conventional applications of the laser. In the past two decades, femtosecond laser ablation [3] was shown to exhibit unique capabilities for micro- and nano-machining in a variety of materials, including transparent materials [4]. Machining platforms based on ultrafast fiber lasers was reported recently [5].

Ytterbium (Yb)-doped fiber-based laser systems [6–8] are currently the laser system of choice for the applications mentioned above. This is primarily due to their efficiency, broad gain bandwidth, and operational wavelength near 1,060 nm (that of Nd: YAG lasers, one of primary workhorses of the industry) [8]. Figure 3.1 shows the energy level diagram of Yb-doped silica fiber and the corresponding absorption and emission spectra. The laser transitions occur between the sublevels of $^4F_{5/2}$ and $^4F_{7/2}$ states in Yb-doped silica. YDF has a very broad absorption and emission band and can be pumped efficiently by 915 nm or 975 nm laser diode. Absorption at 975 nm is much stronger than that at 915 nm though its bandwidth is comparatively narrow. As a result, relatively complicated temperature stabilization schemes are required for the pump laser diodes emitting at the wavelength of 975 nm versus that at 915 nm. The fluorescence lifetime of the upper laser level in YDF, $\tau_f = 0.8$ ms.

C.-L. Pan (✉) · A. Zaytsev · C.-H. Lin · Y.-J. You
Department of Physics, Institute of Photonics Technologies, National Tsing Hua University, Hsinchu, Taiwan
e-mail: clpan@phys.nthu.edu.tw
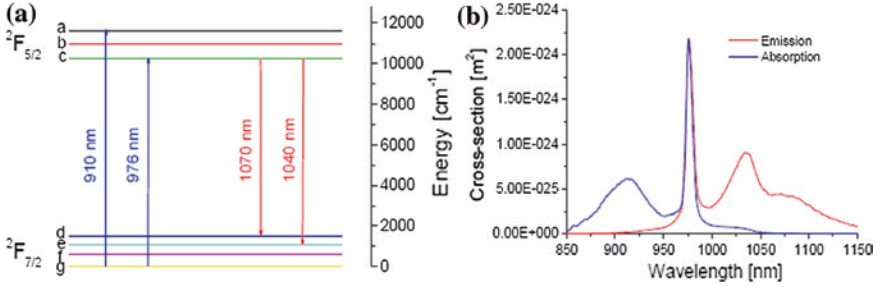
Fig. 3.1 Energy level diagram (**a**) and Absorption (*solid*) and emission cross-sections (*dashed*) of Yb in silica fiber (**b**) as a function of wavelength [6]

Although the long length and tight beam confinement make active fibers suitable for high-power amplification, output of fiber laser systems soon reach peak powers approaching or surpassing thresholds for undesirable nonlinear effects. Therefore achieving high peak power associated with high-power ultrashort pulses with good beam quality constitutes a major challenge. Techniques such as chirped pulse amplification [9, 10] were introduced to reduce peak power in the fiber amplifier and consequently minimize nonlinear effects. This method is well suited for achieving high-energy pulses but typically involves a complex optical arrangement. In practice, direct amplification appears more practical for scaling average power because of its simplicity. This implies that adequate management of nonlinearities in the YDF laser systems tailored to specific applications, e.g., nonlinear frequency conversion, is essential. Nevertheless nonlinearities such as self-phase modulation (SPM) can also be very attractive for the generation of high-power pulses and their subsequent compression.

In this chapter, we describe our recent work on picosecond and femtosecond Yb-doped fiber oscillators and amplifiers. Beginning with a brief description of the master-oscillator power amplifier technology and its capabilities, Sect. 3.2 reviews some of the basic theories useful to understand amplification in fiber amplifiers and describes the various nonlinearities encountered by short pulses propagating in an optical fiber. Such analyses are useful for optimum design of the YDF laser systems. Experimentally, we demonstrated direct fiber amplification of a picosecond passively mode-locked diode-pumped solid-state (DPSS) seeder through a chain of amplifiers using low-cost non-polarization-maintaining (non-PM) YDF. The YDF laser system generated ~11 ps-wide pulses at 250 MHz and an average power as high as 60 W with 73 W pumping. Moreover, the output beam quality was excellent, with $M^2 \sim 1.6$. Detrimental effects such as stimulated Raman Scattering (SRS) and amplified spontaneous emission (ASE) were minimized.

In Sect. 3.3, we showed that a ring-type YDF laser cavity with nonlinear polarization evolution (NPE) port can be configured to generate either continuous-wave mode-locked pulses or noise-like pulses (NLP) with a super-broadband spectrum. Simulation results showing the buildup dynamics for the two regimes were also presented. Self-starting noise-like operation of the laser can be maintained over a

relatively large range of pumping powers (4–13 W). The maximum 3 dB spectral bandwidth of the noise-like pulses was ~48 nm which the output energy can be as high as 47 nJ, limited by optical damage of the fiber components. Generation of supercontinuum (SC) by NLPs propagating through ~100 m of single-mode fiber in the normal dispersion region was also demonstrated. The SC exhibits low threshold (43 nJ) and a flat spectrum over 1,050–1,250 nm.

Finally, we consider amplification of picosecond bursts in Yb-doped fiber amplifiers its impact on frequency conversion applications. A theoretical and experimental comparison between regular pulse trains and pulse bursts shows significant enhancement in terms of conversion efficiencies.

3.2 The MOPA Approach to High-Power Short-Pulse Yb-Doped Fiber Lasers

High-power fiber lasers have been increasingly used in scientific applications [11, 12] as well as material processing [5, 13]. These systems are typically based on master oscillator power amplifier (MOPA) designs. For wavelengths around 1 µm, ytterbium-doped fiber is widely adopted for fiber-based high-power lasers and amplifiers [6]. Yb-doped double-cladding (DC) fibers can be used to build laser systems with output power up to several kilowatts. Such laser systems also exhibit desirable characteristics such as high gain, good efficiency and excellent beam quality [14–19]. For example, C. Zheng et al. reported an all-fiber master oscillator power amplifier (MOPA) system which can generate ~10 ns pulses with energies of 1.2 mJ/pulse [19]. The output beam quality $M^2 \approx 1.4$.

The broad gain bandwidth of Yb-doped fiber is also suitable for the amplification of ultrashort pulses [17, 18]. High-power short-pulse fiber lasers, however, must meet challenges from the onset of unwanted nonlinear effects, like self-phase modulation or stimulated Raman scattering, which limit the maximum output power and degrade output pulse shape and duration. Recently developed photonic crystal fiber (PCF) is able to overcome many of the difficulties mentioned above. PCFs, however, are still very expensive. If a linearly-polarized high-power short-pulse laser is required, it can be based on a master oscillator fiber amplifier (MOFA) design where polarization-maintaining (PM) fibers are used. Further, the PM fibers are well suited to amplify and deliver linearly polarized optical beams to targets with excellent extinction ratio. The PM fibers, however, are much more expensive than conventional non-PM fibers. Further, the thresholds of nonlinear effects in non-PM fibers are higher [20, 21].

A stable seed laser is required for the MOFA. Currently, several research groups adopted fiber mode-locked oscillators as seed lasers [22, 23]. For the moment, however, long-term reliability of modern fiber oscillators is still the main challenge which may affect on the overall MOFA performance. Vertical external-cavity surface-emitting semiconductor lasers (VECSELs) producing nearly transform-limited ps pulses and quasi-diffraction limited beams are suitable

for MOFAs [24]. The output power of VECSEL, however, is well below 1 mW. As a result, multiple amplification stages are required. On the other hand, diode-pumped solid-state (DPSS) lasers can provide transform-limited pulses at moderate power levels. In this section, we presented progress of relatively high-power picosecond MOFAs using non-PM Yb-doped fiber amplifiers seeded by a compact and robust passively mode-locked DPSS Nd:GdVO$_4$ laser which can provide 12 ps duration, at ~200 MHz repetition rate with average power of ~400 mW [25]. An average power of ~28 W at a repetition frequency of 250 MHz was achieved with a single stage of 10-μm-core Yb-doped fiber amplifier in the MOFA. A pulse duration of ~1.4 ps was obtained after recompression with a grating pair [26]. With two stages of non-PM Yb-doped fiber amplifiers, Stimulated Raman scattering (SRS) and amplified spontaneous emission (ASE) can be suppressed by optimizing the active fiber lengths and pumping powers of the amplification stages. We achieved an average output power as high as 60 W, with an optical conversion efficiency 82 % [26]. The SRS peak at 1,120 nm is suppressed by 30 dB. No distortion or other unwanted effects were found at the system output. The output beam quality is measured to be M^2 ~ 1:6.

3.2.1 Theoretical Analysis and System Design

For theoretical analysis and optimum design of the MOFA, we employed the analytical model for rare-earth-doped fiber amplifiers and lasers first proposed by Saleh et al. [27]. Certain simplifying assumptions have to be used in these models: (1) The power extracted by ASE must be negligible. This is valid for a fiber amplifier with input seed power significantly higher than equivalent ASE noise in the channel. (2) The field and dopant distributions must be homogeneous. This is typically the case for single mode doped fiber cores. (3) Excited state absorption must be negligible, which is true for Ytterbium-doped fibers. Further, we neglected the influence of optical feedback on the signal. This is reasonable because angle-cleaved fiber ends were employed in our experimental setup. Following Barnard et al. [28], we can write down the steady-state rate equations for the amplifier as follows:

$$N_1 + N_2 = N_t \tag{3.1}$$

$$\frac{\partial P_p}{\partial z} = \Gamma_p \Big[\sigma_p^e N_2 - \sigma_p^a N_1 \Big] P_p \tag{3.2}$$

$$\frac{\partial P_s}{\partial z} = \Gamma_s \big[\sigma_s^e N_2 - \sigma_s^a N_1 \big] P_s \tag{3.3}$$

$$\frac{N_2}{N} = \frac{(\sigma_s^e + \sigma_s^e)\sigma_p^a P_p P_s^{sat} + \Big(\sigma_p^a + \sigma_p^e\Big)\sigma_s^a P_s P_p^{sat}}{\Big(\sigma_s^a + \sigma_s^e\Big)\Big(\sigma_p^a + \sigma_p^e\Big)\Big(P_p P_s^{sat} + P_p^{sat} P_s^{sat} + P_p P_s^{sat}\Big)} \tag{3.4}$$

In (3.1–3.4), N_t is the doping density of Yb^{3+} ions in the active fiber. N_1 and N_2 are the population densities of lower and upper lasing levels, respectively. P_p is the pump power, z is the spatial coordinate along the fiber axis, P_s is the signal power. σ_s^e and σ_p^e are the emission cross-sections of the signal and the pump light, respectively. Similarly, σ_s^a and σ_p^a are the absorption cross-sections of the signal and the pump light, in that order. Other parameters used include the lifetime of the lasing transition, τ; the overlap integral of pump and signal, Γ_s and Γ_p; the effective area of the fiber core, A; Planck constant, h; the velocity of light, c. Equations (3.2–3.4) can be solved analytically and expressed as follows [29]:

$$\frac{P_p^{IN}}{h\nu_p}\left(1-\left(\frac{G}{G_{\max}}\right)^{\delta}\right) = \frac{P_s^{sat}}{h\nu_s}\left(\Gamma_s N\sigma_s^a L + \ln G\right) + \frac{P_s^{IN}}{h\nu_s}(G-1), \quad (3.5)$$

where $\delta = \frac{P_s^{sat}/h\nu_s}{P_p^{sat}/h\nu_p}$ is the ratio of saturation powers, G is a signal gain, $G_{\max} = \exp\left[\left(\frac{\Gamma_p N\sigma_p^a}{\delta} - \Gamma_s N\sigma_s^a\right)L\right]$ is the maximum gain. P_p^{in}, P_s^{in} are total power of pump and signal lights at the input of the amplifier, respectively.

Using the formula summarized above and the physical parameters of Yb-doped double-cladding fibers provided by fiber manufacture (Liekki), we calculated the output power as the function of active fiber length (see Fig. 3.2). The calculations were made assuming fiber's cross-sections from [6], 100 mW of average seed power and pumping power at 20 W. These are summarized in Table 3.1.

Simulations indicated that the optimal fiber length for a 10-μm-core fiber amplifier stage would be ~10–12 m. Similarly, the optimal fiber length of 30-μm-core diameter fiber is ~3–5 m. These are plotted in Fig. 3.2.
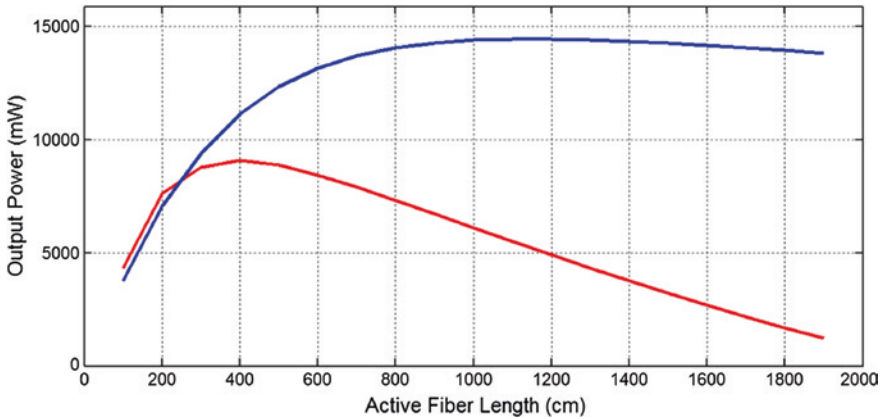
Fig. 3.2 Simulation for the dependence of output power as a function of fiber length of two different Yb-doped fibers (YB1200-10/125DC, Liekki with 10 μm core diameter—*blue curve*, and YB1200-30/250DC, Liekki with 30 μm core diameter—*red curve*) for single stage amplification. The input power and pump power are assumed to be 100 mW and 20 W, respectively, for both fibers

Table 3.1 Main parameters of the 10-μm-core Yb-doped double-clad fiber

Parameter	Value	Parameter	Value
N	9.5×10^{25} m^{-3}	Γ_s	0.82
τ	0.84 ms	Γ_p	0.01
σ_s^a	5×10^{-27} m^2	λ_p	915 nm
σ_s^e	3.4×10^{-25} m^2	λ_s	1,064 nm
σ_p^a	7.8×10^{-25} m^2		
σ_p^e	3.1×10^{-26} m^2		

In comparison, the 10-μm-core fiber amplifier stage with optimal fiber length appears to exhibit higher power than the optimized 30-μm-core fiber amplifier stage (see Fig. 3.2). The above analysis, however, does not consider the nonlinear effects such as the stimulated Raman scattering (SRS) and self-phase modulation (SPM). These nonlinearities are non-negligible at high signal powers and result in pulse distortion and other undesirable consequences. A rough estimate shows that the Raman threshold for our input condition and the optimal fiber length is below a peak power of 2.3 kW or an average signal power of 7 W. Therefore, the output power of a single 10-μm-core fiber amplifier stage is limited in order to avoid significant pulse distortion and efficiency degradation. On the other hand, the output power of a 30-μm-core fiber amplifier stage is relatively small (~0.4 W, see Fig. 3.2) with the same input signal and pump power. Due to the large core size, a seed signal power higher than 1 W is required to achieve a good pump to signal conversion efficiency. It is reasonable, therefore, to consider the design of a dual-stage amplifier system, using a length of 10-μm-core fiber as the preamplifier and another length of 30-μm-core fiber for the main amplifier.

For optimization of such a dual-stage fiber MOPA system, we first used the formalism above to optimize each stage separately in order to achieve the highest gain. It is well known that larger core size and shorter fiber length will increase the nonlinear thresholds. Therefore, effects such as SRS and SPM are expected to be more likely to happen in the first or the preamplifier stage, which employs fibers of smaller core size. The SPM will broaden the spectrum, which is distributed about the signal wavelength. The SRS will create new wavelengths which are far from the signal. The signal power limitation of SRS is more serious than the SPM. Using the formula in [30] and assuming a Raman gain coefficient $g_R \sim 3.2 \times 10^{13}$ mW^{-1} [31], we estimated that the SRS threshold is ~2.3 kW for a 10-μm-core fiber with optimized length of 7 m. For a 30-μm-core-fiber and ~5 m in length, the SRS threshold increases by a factor of more than ten to ~27 kW.

In our design, we set the output power of the preamplifier stage at ~3 W, which is below the SRS threshold for the 10-μm-core fiber preamplifier. Assuming 2 W of power was injected into the 2nd or main-amplifier stage. In Fig. 3.3, we have calculated and plotted the normalized gain of the first stage (10-μm-core fiber) and second stage (30-μm-core fiber) of MOPA as a function of their respective
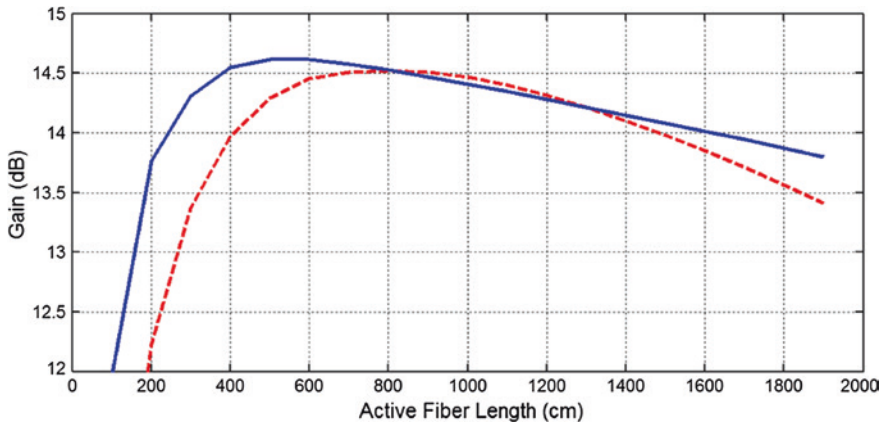
Fig. 3.3 Simulated gain as a function of the fiber length of the 1st (*dashed red curve*) and 2nd (*solid blue curve*) stage amplifiers in a dual-stage Yb-doped fiber amplifier. The core diameters are 10 and 30 μm, respectively. The input signal power is 100 mW in the 1st stage and 2 W in the 2nd stage, respectively. The pump power is 5 W in the 1st stage and 80 W in the 2nd stage

length. The optimal fiber length of the main amplifier stage is ~5 m (see solid curve of Fig. 3.3). Actually, the optimal fiber length of the 10-μm-core fiber can be reduced in the dual-stage amplifier system. In order to achieve an output power of ~3 W in the preamplifier stage, the needed fiber length is only ~5 m (see dashed curve of Fig. 3.3), further reducing the possible detrimental nonlinear effects.

3.2.2 Picosecond Laser Seeder

For the master laser, we designed and constructed a compact and robust passively mode-locked DPSS Nd:GdVO$_4$ laser which can provide 12 ps duration, at ~250 MHz repetition rate with average power of ~400 mW [25].

The laser employed a linear cavity, as shown in Fig. 3.4. A Brewster-cut Nd:GdVO$_4$ laser crystal with a dopant concentration of 1.5 % Nd and the
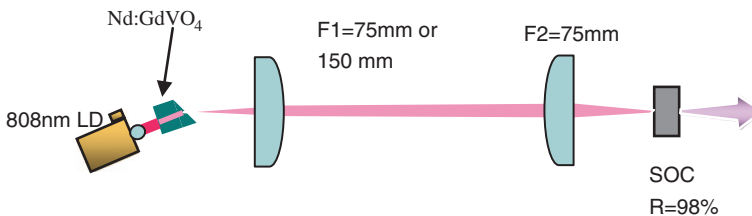
Fig. 3.4 Schematic of the DPSS laser. *SOC* Saturable Output Coupler

dimensions of $2 \times 2 \times 3$ mm^3 was used. One of its light-passing facets was coated for high reflection (HR) at the lasing wavelength of 1,064 nm and high transmittance (HT) at the pump wavelength of 808 nm, the other side (Brewster-cut) was coated for HT at 1,064 nm. The laser was pumped by a C-mounted 808 nm laser diode (LD) with integrated fast axis collimator and maximum output power of ~2 W. For simplicity and cost reduction, we did not use any optics for re-imaging the pumping spot into the laser crystal. Instead, we placed laser crystal at a short (~0.2 mm) distance from the LD chip surface. The LD and Nd:GdVO$_4$ crystal, wrapped with indium film, were embedded in a copper heat sink that is part of a compact module [25]. The cavity contains a saturable output coupler (SOC, made by BATOP Gmbh, Weimar, Germany) that serves as the saturable absorber as well as the output coupler. In our experiments, we used a SOC of 2 % transmission not to achieve the lowest possible threshold but to find the laser condition optimally matched with the laser diode used for pumping.

The HR-coated crystal's facet, two HT-coated convex lenses (F1 and F2), and the SOC form the two-mirror cavity of the laser. We adjusted the cavity length from 0.6 to 1 m and experimented with F1 lens of which the focal lengths, f_1, were 75 and 150 mm, respectively. The focal length of F2 was fixed at 75 mm. The calculated and experimentally measured critical average powers P_{out} for several variations of the cavity design are summarized in Table 3.2. Here, P_{out} is the minimal output average power corresponded to the CW mode-locked state [25]. An example of measured laser spectrum in the mode-locked state is shown in Fig. 3.6a.

We found that measured P_{out} is slightly higher than theoretically predicted values. This is tentatively attributed to additional intracavity loss mechanisms, e.g., reflection losses, scattering losses, mode areas mismatch. From Table 3.2, it is clear that increasing the cavity size and using F1's with shorter focal length result in increasing intracavity pulse energy, reduced mode-locking threshold, and suppression of Q-switching instabilities. On the other hand, longer cavity length is undesirable for the design of a compact system and also reduces the repetition rate.

In Fig. 3.5, we have plotted laser output powers versus pumping power for different cavity configurations. Note that the cavity with $f_1 = 150$ mm exhibited higher efficiency than ones with $f_1 = 75$ mm. We attribute this to enlarging the mode area and better mode matching with the pumping beam in the former. The improvement in efficiency, however, is accompanied by higher mode-locking thresholds.

The envelope of the interferometric autocorrelation trace with the Gaussian fitting curve is shown in Fig. 3.6b. From fitting parameters, we can estimate the
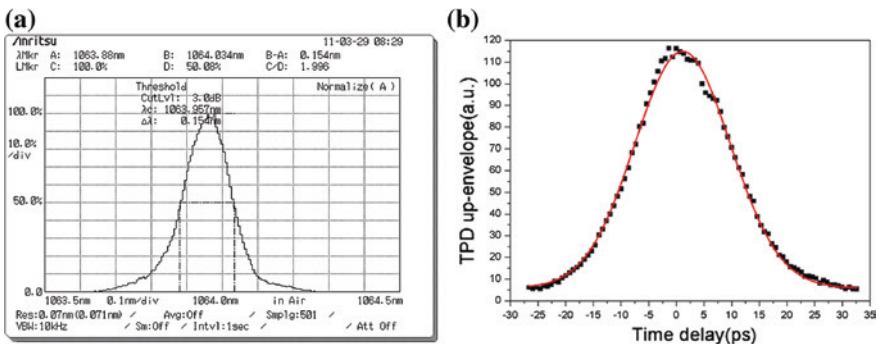
Table 3.2 Calculated and measured critical average powers

Cavity length	1 m	60 cm	1 m	60 cm
f_1 (mm)	75	75	150	150
Calculated P_{out} (mW)	170	250	340	510
Measured P_{out} (mW)	185	260	350	NA
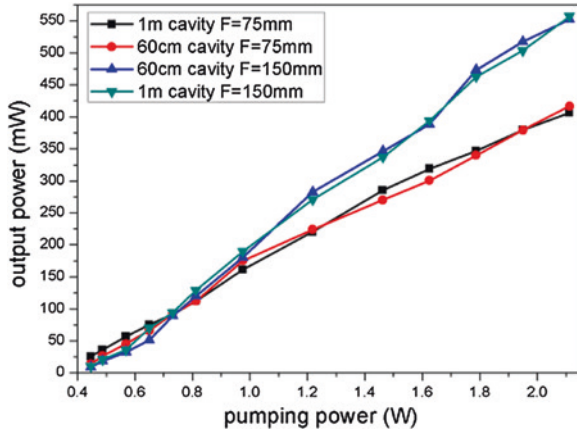
Fig. 3.5 Output power versus the pump power curves for cavity configurations listed in Table 3.1

Fig. 3.6 **a** Measured optical spectrum of mode-locked Nd:GdVO$_4$ laser; **b** The measured envelope of an interferometric autocorrelation trace and its *Gaussian fitting curve*

pulse duration at ~12 ps. The calculated time-bandwidth product 0.49 obtained by using the measured optical spectrum (see Fig. 3.6a) shows that DPSS laser irradiates almost transform-limited pulses.

In the case of optimal condition (60 cm cavity and F$_1$ = 75 mm) the laser generates ~12 ps pulse trains at ~250 MHz (see Fig. 3.7) with an average output power P_{out} of about 260 mW when the pumping power is 1.3 W.

For the condition that the output power of the laser was ~270 mW which was slightly higher than that of the CW mode-locking threshold, the fluctuation of average output power for 11 h operation was recorded (see Fig. 3.8). For comparison, we also presented the fluctuation data if active cooling was used to stabilize the temperature the basement of LD and laser crystal mount at 20 °C (red dot).
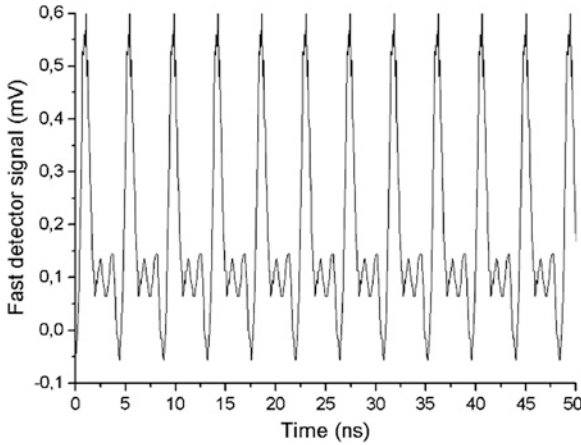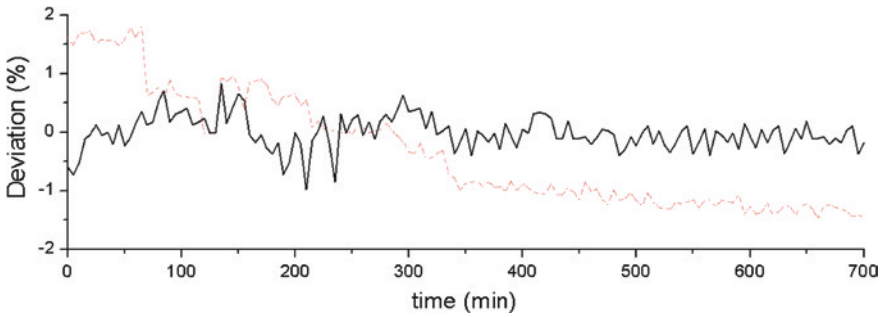
Fig. 3.7 The pulse train at 60 cm cavity

Fig. 3.8 Long-term fluctuations of laser output with active cooling (*solid*) and without of active cooling (*dot*)

We can observe from Fig. 3.8 that the average power fluctuations in long-term operation do not reach more than ±2 % which was slightly higher than in the case when active cooling was used (±1 % fluctuations). We attribute this superior performance to several factors. First of all, we achieved good thermal stability through reduction of excessive absorbed heat and good thermal sinking of the pumping module consisting of the laser crystal and the pumping LD [25]. Secondly, the cavity configuration is simple and thus mechanically stable. The last feature also suggests easer alignment of laser cavity.

3.2.3 Multi-Stage Fiber Laser Amplifiers

The experimental setup of the proposed high power picosecond laser system is shown schematically in Fig. 3.9 [32]. It is constructed in a dual-stage MOFA configuration. The mode-locked DPSS seed laser has been reported previously (see Fig. 3.4).
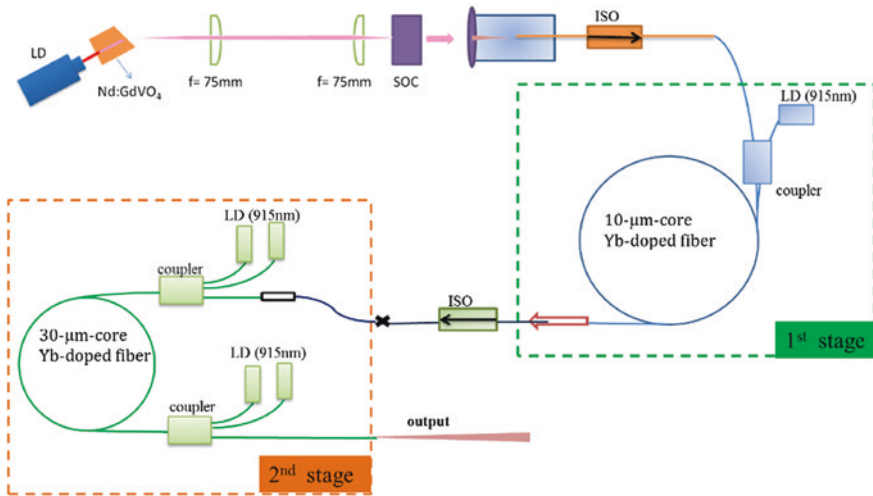
Fig. 3.9 Schematic drawing of the MOFA system. *LD* laser diode; *SOC* saturable output coupler, *ISO* isolator

In the two fiber amplifier stages, all fibers are non-PM fibers. We used the theoretical model in Sect. 3.2.1 to determine the optimum fiber length with a given pump power for maximum power output while minimizing undesired nonlinear effects. Thus, a 7-m-long, 10-μm-core double-cladding Yb-doped fiber (YB1200-10/125DC, Liekki) was used in the preamplifier stage. The absorption per unit length of this fiber 1.8 dB/m at 915 nm. Another 5-m-long 30-μm-core double-cladding Yb-doped fiber (YB1200-30/250DC, Liekki) was used in the main-amplifier stage. The absorption per unit length for either fibers was 3.6 dB/m at 915 nm. A $(2 + 1) \times 1$ optical combiner was used to couple the signal and pumping light together before being sent into the active fiber. The signal fiber core size of the combiner was matched with that of the active fiber core. Due to the large wavelength tolerance of absorption near 915 nm, pump laser diode at this wavelength were used in order to provide stable absorption in the active or gain fibers [33]. Between the two stages, we used a polarization-independent optical isolator. This is essential to prevent the reflection from the output end and avoid self-oscillation in the amplifier stages. At the pigtail of fiber amplifiers, we also used angle-cleaved ends to prevent any feedback. A home-made second-harmonic intensity autocorrelator and an optical spectrum analyzer (MS9780A, ANRITSU) were used for pulse characterization. The beam quality was determined by a home-made M square measurement setup.

In the main or second amplifier stage, either forward or backward pumping is possible. The pumping efficiencies for the two cases are shown in Fig. 3.10. Clearly, backward pumping is superior. This is consistent with reports by previous workers [34, 35].

Fig. 3.10 Experimentally
measured output power of the
main-amplifier as a function
of the pumping power for
forward (*black squares*)
and backward (*red circles*)
pumping schemes
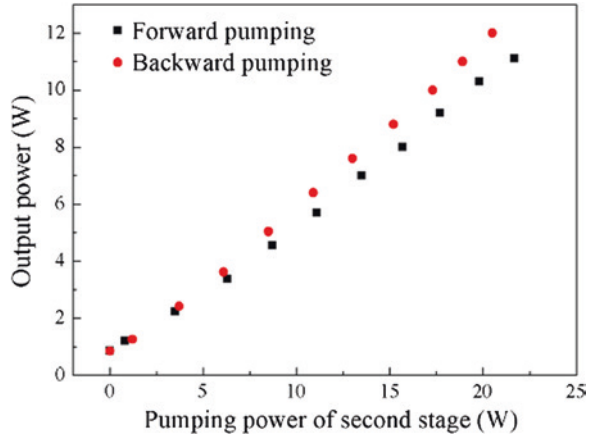

3.2.4 MOPA Performance

The output power of the first stage fiber amplifier or the preamplifier is plotted as a function of pumping power in Fig. 3.11a. The solid curve is the theoretical prediction according to (3.5). A maximum average output power of 28 W was obtained by employing a 7-m-long 10-μm-core double-cladding Yb-doped fiber pumped at 50 W [26]. The corresponding optical conversion efficiency is ~56 %. At low pumping powers (below 12 W), the experimental results are in good agreement with the theoretical curve. At higher pumping powers, the experimentally measured output powers are lower than the simulation results. This is attributed to the SRS effect. Simple estimation shows, when the pumping power is up to 13 W, the peak power from the preamplifier is $\leq$2.2 kW, which is close to the estimated SRS threshold of 2.3 kW (see Sect. 3.2).

Figure 3.11b shows the output spectrum of the preamplifier for several values of the pump power. The peak at 1,120 nm wavelength, corresponding to the first Raman Stokes line [21], became visible when pumping power reaches 13 W. Larger pump power will cause more serious Raman amplification in the spectral region around 1,120 nm. As a result, signal depletion at 1,064 nm became evident. This is not desirable.

Moreover, at high pump powers, self-phase modulation (SPM) significantly broadens the output spectrum. On the one hand, SPM is unwanted phenomena because it may cause pulse distortion. On the other hand, it opens the way to recompress the pulse by employing an anomalous dispersion line. In [26] we demonstrated such a possibility. A gratings pair in Littrow configuration was used to compensate the positive phase shift in fiber. We found that the minimal full-width half-maxima (FWHM) of autocorrelation trace of the pulses was ~2 ps. This was observed at a grating separation of ~30 cm. A comparison between autocorrelation traces at 10 W average output power measured on the amplifier output before
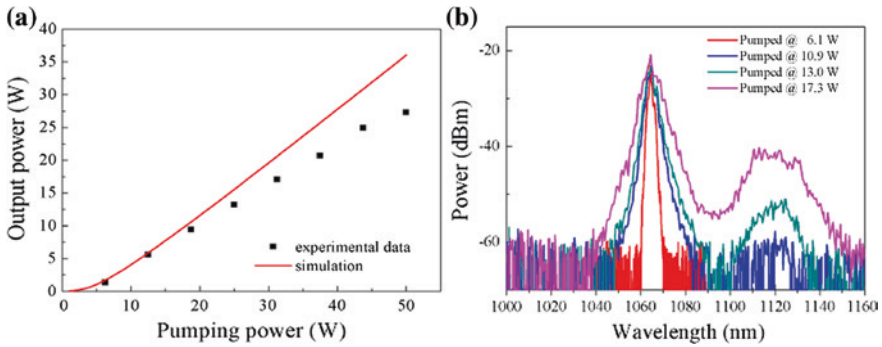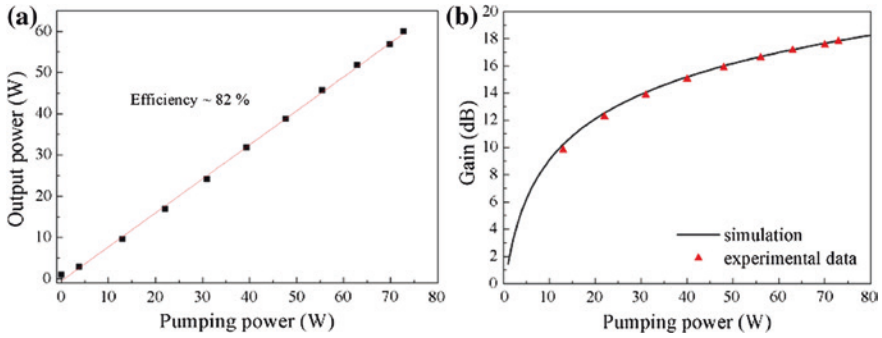
Fig. 3.11 Performance of the preamplifier: **a** Output power versus (*forward*) pumping power. The *solid curve* is the theoretical prediction according to (3.5); **b** optical spectrum of the output of the preamplifier at different pumping power levels
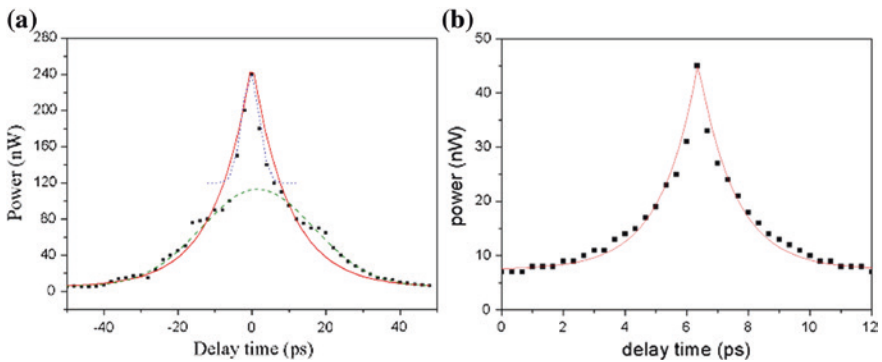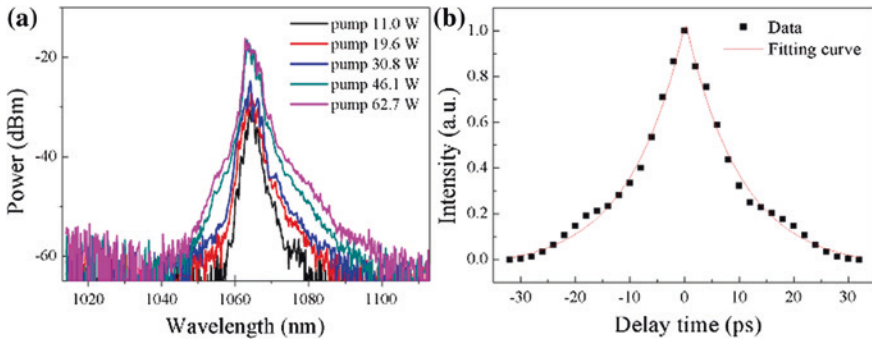

Fig. 3.12 Measured autocorrelation trace of the amplified **a** and recompressed **b** pulses at 10 W average power output

and after gratings compressor is shown at Fig. 3.12. Fitting curve assuming double exponential pulse shape matches the experimental data very well for both cases. From extracted parameters we can estimate that the pulse width duration at ~12 ps before and ~1.6 ps after compression, respectively. Further increasing of output power of the pre-amplifier beyond 10 W results in pulse broadening that cannot be compensated by adjusting the gratings compressor. Obviously, at the higher power levels the spectrum shape at the amplifier output is beyond typical SPM and in order to get shorter pulses the high-order nonlinearity should be taken into account and more comprehensive study should be done.

To obtain higher output power and suppress the SRS effect, the 30-μm-core fiber was chosen for the gain fiber of the second amplification stage. About 2 W of average power was measured at the input of the main or second-stage amplifier (after the second fiber-type optical isolator). This is significantly below the SRS

Fig. 3.13 Performance of the 2nd-stage or main amplifier with 30-µm-core fiber: **a** experimentally measured output power versus pumping power; The *solid red line* is the fitting curve, corresponding to an efficiency of ~82 %. **b** the comparison of simulated and experimentally measured gain

Fig. 3.14 Spectral and temporal characteristics of the output of the 2nd-stage or the main amplifier: **a** optical spectra as a function of pumping powers; **b** the second-harmonic intensity autocorrelation trace of the pulse train

threshold. The pump-power scaling of the output of the main amplifier stage is shown in Fig. 3.13a. With 73 W of pumping power, an average output power of 60 W or a peak power ~21.8 kW was measured at the output of the main amplifier. The corresponding optical conversion efficiency was 82 %. The simulation results, according to (3.5), are plotted as the solid curve in Fig. 3.13b. Clearly, the experimental results are in good agreement with the simulation curve.

Figure 3.14a above shows the spectrum of the MOFA output as a function of the pumping power. The spectrum broadens from 1.6 to 6.4 nm when the pumping power was 62.7 W. This is in good agreement with theoretical estimation of the broadened spectral width, which is 8 nm. The spectral broadening is attributed primarily to self-phase modulation in the active fiber.

The peak power of the MOFA output was lower than that for the SRS threshold, estimated to be 27 kW. The SRS was therefore negligible in our MOFA system. This is consistent with the observation that SRS peak is at least 30 dB smaller than the main peak at the highest pumping power level used (see Fig. 3.14a). Therefore, most of the output power concentrates at the seed laser wavelength. The second-harmonic intensity autocorrelation trace of the MOFA output is shown in Fig. 3.14b. It can best be fit by a double-exponential function. The corresponding FWHM of the electric field waveform of the pulse was ~11 ps (see Fig. 3.14b). This is about the same as that of the seed laser.

The beam quality or propagation factor (M^2) of the MOFA, as measured by a home-made setup, was ~1.6 (See Fig. 3.15).

For now, the output power of our MOFA system was limited by the pump power. That is, the main amplifier had not yet reached saturation. Making sure that we operate below the SRS threshold of the main amplifier stage, we estimate that the maximum output power of the present MOFA can reach 75 W, if we provide enough pump power up to ~92 W.

In summary, an average power as high as 60 W with 73 W of pumping was achieved with an optimized pico-second ytterbium-doped non-PM fiber-based dual-stage amplifier (MOFA) system seeded by a compact modelocked solid-state laser. The corresponding optical conversion efficiency is 80 %. The laser system generates a steady pulse train at the repetition rate of 250 MHz with pulse width of 11 ps or a peak power of 21.8 kW. The output beam quality $M^2 \approx 1.6$. The length and pumping power for the Yb-doped fibers were optimized to suppress stimulated Raman scattering (SRS) and amplified spontaneous emission (ASE) while maintaining desirable output characteristics.

Fig. 3.15 Beam profile measurement of the MOFA system. W_x and W_y are the beam radii in horizontal directions, respectively
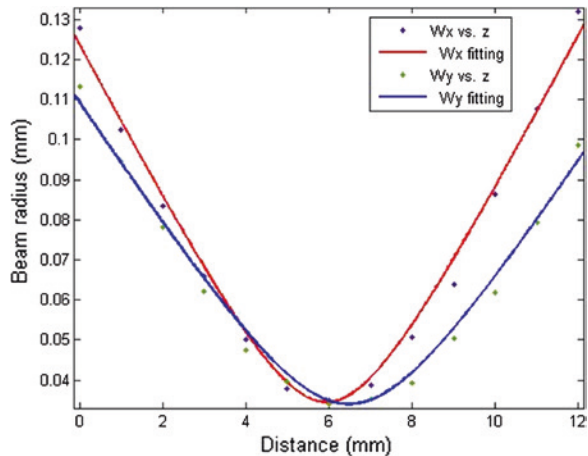
3.2.5 Mode-Locked Yb-Doped Fiber Laser

Mode-locking technique is commonly employed to generate ultrashort pulse train from a laser oscillator. One popular approach, passive mode-locking is achieved by using a fast saturable absorber and a gain medium with broad gain bandwidth. In the fiber laser, fast saturable absorber (SA) action can be realized using nonlinear polarization evolution (NPE) [36] due to the optical Kerr effect in the fiber. It can be easily implemented with the help of a polarizing beam splitter (PBS) and a few wave plates as shown in Fig. 3.16. Fast saturable absorption action based on NPE can be explained as follows. The linear polarization after the PBS is made elliptical using a quarter wave plate. As the pulse propagates through the fiber, the axes of the polarization ellipse rotate continuously from the peak to the valley of the pulse due to Kerr nonlinearity. At the fiber exit, the polarization directions are adjusted using a quarter wave and a half wave plates so that the peak of the pulse sees high transmission and the wings are attenuated.

In this way, the NPE acts like a fast saturable absorber and leads to the intensity discrimination and narrowing of the pulse. Usually, a unidirectional ring cavity is required for NPE to be effective and for self-starting operation of the laser. There are, however, several important characteristics that distinguish NPE from the more traditional SESAM mode-locking mechanism. First of all, it differs from a saturable absorber material since high intensities can "overdrive" the transmittance, causing the negative slope regions (see Fig. 3.17). Secondly, the NPE transmission function becomes periodic at high energies. This can be explained by the dependence of NPE on the angle of rotation of the elliptically polarized light. This over-driving of the mode-locking creates limitations in the attainable pulse energy. Further, because it is a polarization-based mechanism, NPE is extremely sensitive to environmental changes. Any disturbances (mechanical, temperature) may cause unstable operation.

According to the fluctuation mechanism of mode-locked pulse generation using a saturable absorber, there are two stages of pulse formation. In the linear stage, a large number of axial modes interfere to create a strong burst of intensity
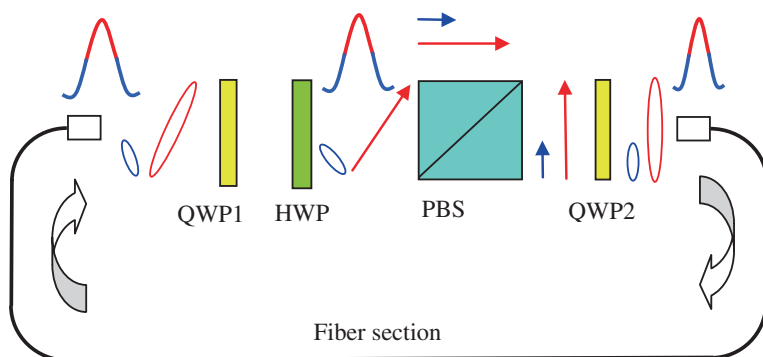
Fig. 3.16 Fast saturable absorption action based on nonlinear polarization rotation

Fig. 3.17 Transmittance of an artificial saturable absorber such as NPE port versus intensity
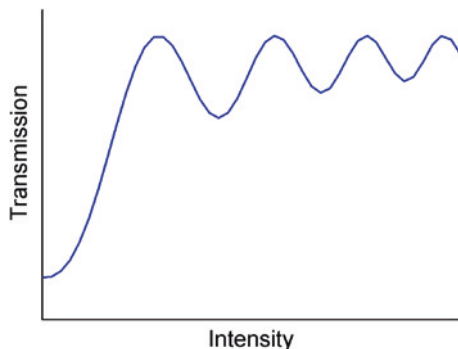

fluctuation. In the nonlinear stage, when the saturable absorber is bleached, the most intense fluctuation peak is compressed in time and amplified further. Pulse narrowing by the SA is balanced by the gain filtering effect of the active medium leading to the formation of bandwidth-limited mode-locked pulse [21]. In a fiber laser, however, the stable pulses will be generated only when the interplay of non-linearity, gain and dispersion will be such that the chirping in the pulse can be managed with the help of a dispersion compensating elements, like a grating pair, so that the pulse shape repeats itself after each round trip. Hence, a prior simulation is required for designing the mode-locked fiber oscillator to find the operating regime at which the stable mode-locked pulses can be evolved from the initial intensity noise fluctuations. The propagation of noise fluctuation in each segment of the oscillator can be modeled by the generalized coupled nonlinear Schrodinger equations (NLSE) given by [37]

$$\begin{cases} \frac{\partial A_x}{\partial z} = i\gamma \left\{ |A_x|^2 A_x + \frac{2}{3}|A_y|^2 A_x + \frac{1}{3}A_y^2 A_x^* \right\} + g(E_{pulse})A_x - \frac{i}{2}\beta_2 \frac{\partial^2 A_x}{\partial t} \\ \frac{\partial A_y}{\partial z} = i\gamma \left\{ |A_y|^2 A_y + \frac{2}{3}|A_x|^2 A_y + \frac{1}{3}A_x^2 A_y^* \right\} + g(E_{pulse})A_y - \frac{i}{2}\beta_2 \frac{\partial^2 A_y}{\partial t} \end{cases}. \quad (3.6)$$

Equation (3.6) also includes the effects of gain and gain filtering due to the finite gain bandwidth. If the parameters given for the oscillator are favorable for mode-locking, then a stable pulse shape will evolve from the initial intensity noise fluctuation after many round trips.

Various types of ultrashort pulse shapes can be generated by mode-locking Yb-doped fiber oscillator by adjusting the interplay of dispersion, nonlinearity and gain. YDF oscillator can be operated mainly in three different mode-locking regimes, namely stretched pulse, similariton and all-normal dispersion depending on the net value of GVD in the cavity as discussed below:

Stretched pulse mode-locked YDF laser: The stretched pulse YDF laser was first demonstrated by Lim et al. [38]. It is so named because the mode-locked pulse undergoes periodic stretching and compression in each round trip. Under the condition of negative GVD, the natural solution of (3.6) is a hyperbolic secant pulse. Such pulses are referred to as soliton pulses as the negative GVD and the
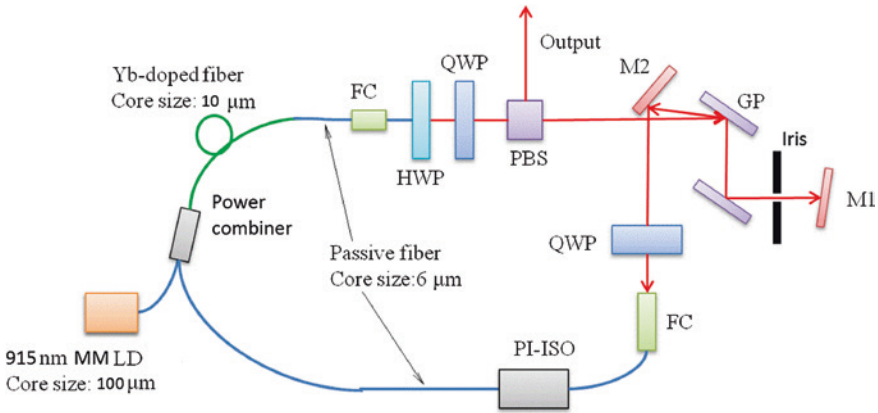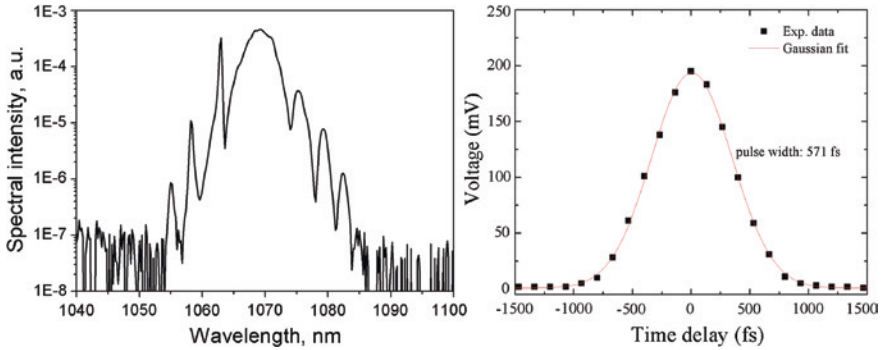
Fig. 3.18 Schematic of dispersion managed soliton fiber laser: *FC* fiber coupler; *HWP* half-wave plate; *QWP* quarter-wave plate, *GP* grating pair; *PI-ISO* isolator; M1, M2, mirrors

nonlinearity cancel each other leading to the pulse shape whose temporal and spectral profiles do not change with the propagation distance. Under normal dispersion (for wavelength ~1 µm in silica fibers), conventional soliton pulse cannot be generated. Instead, soliton-like pulses known as the dispersion managed (DM) soliton or stretched pulses can be formed by employing a negative dispersing element like a grating pair in the cavity to cancel the phase introduced by the positive GVD and SPM in the fiber [39].

The schematic of a typical stretched pulse YDF laser is shown in Fig. 3.18 [40]. The laser set-up comprises of a segment of single-mode silica fiber followed by a gain segment. NPE is implemented by a PBS and wave plates. A grating pair in the near-Littrow configuration is placed after the PBS to provide negative dispersion in the cavity. The grating is therefore also known as the dispersive delay line (DDL). The net GVD of the cavity is kept slightly positive. An optical isolator is placed in the air space to ensure unidirectional operation of the laser so that the mode-locking process is self-starting. By adjusting the wave plates, stable mode-locked pulses are readily observed. As the pulse propagates through the SMF and the gain segment, the temporal and spectral widths increase with a positive chirp due to the interplay of GVD and nonlinearity. The pulse becomes negatively chirped after passing through the grating pair. Afterwards, propagation in the SMF adds positive dispersion. This leads to spectral and temporal compression of the pulse and bringing it back to its original shape. The output can be taken directly from the NPE ejection port (Fig. 3.19).

In Fig. 3.20, we show the simulation results of the temporal and spectral buildup dynamics of the stretched pulse mode-locked YDF laser. It illustrates the following process: An initial burst of broadband thermal noise photons serves as the seed starting the laser oscillation. The nonlinearity begins to affect propagation of these noise photon burst only after its flux reaches some value (after few

Fig. 3.19 Spectrum (*left*) and autocorrelation trace (*right*) of the dispersion-managed soliton fiber laser like on Fig. 3.18
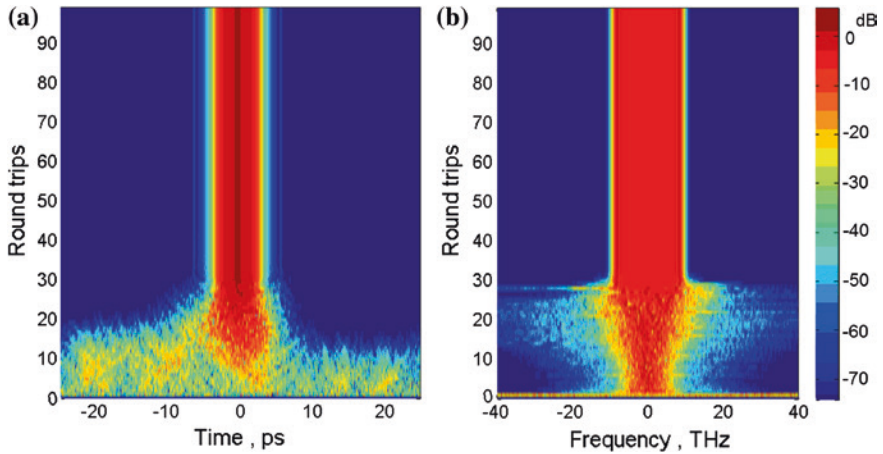
Fig. 3.20 Simulated build-up dynamics in time **a** and spectral **b** domains of the fiber oscillator based on NPE SA

roundtrips). Then, NPE mechanism gets involved in the pulse formation process. Finally, regular pulses start to circulate in the laser cavity after several tens of round trips.

The pulses are chirped inside the gain segment in a stretched pulse mode-locked YDF laser. As a result, their energies can be scaled up significantly as compared to that of a soliton pulse. Pulse energy of 5 nJ with a compressed pulse duration of 50 fs has been demonstrated from a stretched pulse YDF laser [41]. The shortest pulse duration of 33 fs from a YDF oscillator was also achieved using the stretched pulse configuration by employing simultaneous third-order-dispersion (TOD) compensation [42]. Further energy scaling is unfortunately limited by the wave breaking of the pulses and over-driving of the NPE due to strong nonlinear effects in the fiber.

Similariton laser: Similariton pulses are the asymptotic solution of the NLSE under normal dispersion. That is, if certain conditions are satisfied, any input pulse shape would evolve as a parabolic one after propagating through the fiber [43]. Mathematically, a similarton pulse has a parabolic temporal shape as well as quadratic phase profile. This would naturally lead to linear frequency chirping. A similariton pulse propagates through the fiber in a self-similar manner. That is, the spectral and temporal profiles are always a scaled version of itself even in the presence of high gain or loss. The configuration of this class of lasers is similar to that of the dispersion managed soliton laser (See Fig. 3.18) but has a large amount of net positive GVD obtained by increasing the undoped single-mode fiber length. The purpose of the grating pair is to compress the pulse to its initial width. For the self-similar pulse to evolve to the steady state, its pulse energy should be high enough (requirement of high gain) and should pass through long distance in the undoped fiber. It should be noted that the pulse always has a linear positive chirp even in the presence of negative dispersion of elements such as the grating pair. The temporal shape of a similariton pulse has a quadratic phase profile, a unique signature of such a pulse. Therefore, similariton pulses are best-suited for fiber amplifiers as they are resistant to wave-breaking even in the presence of strong nonlinearity. Due to the linear chirp, there is no limitation on energy scaling as the pulse would not suffer from wave-breaking.

All-normal dispersion (*ANDi*) *laser*: An all-normal dispersion laser is perhaps the simplest kind of mode-locked Yb-doped fiber oscillators. There is no need for components for dispersion compensation such as the grating pair [44]. Typically, the dispersion in the cavity of an ANDi laser is managed by a narrow-bandwidth interference filter. The wings of a highly chirped pulse will be cut by the filter, resulting in a shorter pulse. Thus, the filter leads not only to pulse width management but also to a strong self-amplitude modulation by transmitting the peak of the pulse and attenuating the wings. Further, the central wavelength of the pulse can be tuned by changing the peak transmission wavelength of the filter. As there is no negative dispersing element, the net GVD in the cavity is very high and positive. As the pulse propagates through the SMF, the pulse spectrum broadens significantly and develops a structured profile with steep edges due to strong SPM. The narrow band filter cuts down the edges of the spectrum and hence the pulse wings to restore it to its initial form. Even with highly structured spectral profile, the temporal shape is smooth with a linear chirp near the center of the pulse. The breathing of spectrum and the temporal shape are not as large as the other regimes of the mode-locking.

3.2.6 Noise-Like Pulse Generation from a YDF Laser

There has been increasing interests recently in the study of a special regime of passively mode-locked fiber lasers, that of the so-called noise-like pulses [45–49]. These pulses are relatively long (sub-ns) wave packets, which exhibit a fine inner structure of sub-ps pulses with randomly varying amplitude and duration [50, 51].
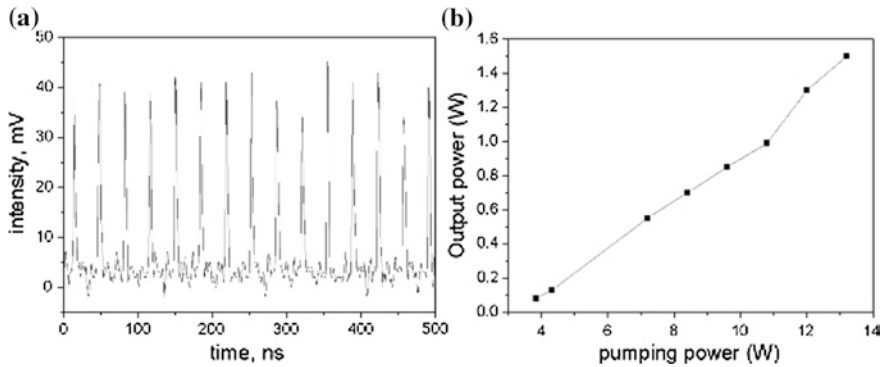
Fig. 3.21 Oscilloscope trace of the train of noise-likes pulse (**a**); Output power of the noise-like pulse laser versus pumping power (**b**)

The properties of such kind of pulses include: (1) a very large optical bandwidth (usually of several tens of nm); (2) a double-scaled autocorrelation trace with a sub-ps peak riding a wide sub-ns pedestal; (3) low temporal coherence. Moreover, it was found [50] that narrow peak in the autocorrelation trace of noise-like pulses or NLPs could be maintained even after the pulses propagated through a long dispersive medium. This unique property of noise-like pulses contrasts drastically with the propagation characteristics of transform-limited pulses of similar bandwidth. Light sources with such narrow autocorrelation trace and broadband spectrum which can propagate for a long distance are very useful in such areas as optical metrology (for example, in optical coherent tomography or lidar), where short coherence lengths are essential and ultimately required [52]. It was also demonstrated [53, 54] that amplified noise-like pulses could be successfully used for SC (supercontinuum) generation.

Recently, it was found [45–47, 49, 55] that different laser structures can operate in noise-like regime. The current challenges are focused on new wavelength bands [47], higher pulse energy generation [48, 55] and tuning the temporal and spectral properties of the noise-like pulses [45, 51]. To the best of our knowledge, 28 nJ as the highest pulse energy was achieved for noise-like pulses [48]. This was achieved using an ultra-long laser cavity (>100 m).

In our studies, we used a modified ring fiber laser cavity, similar to those used for the stretched pulse mode-locked YDF laser (see Fig. 3.18). The same components, e.g., an Yb-doped fiber, NPE-port, dispersive delay line, and an isolator, were employed. Details can be found in [40].

After the single-pulse operation was obtained in this laser, we tuned one of the wave plates while holding all the other experimental conditions unchanged. It is possible to shift the laser operation from the conventional single-pulse operation into the noise-like pulse emission regime. This behavior was also reported by previous workers [46, 48]. Figure 3.21a shows the oscilloscope trace of the laser output as measured by a fast InGaAs detector. It is found to be typical for noise-like
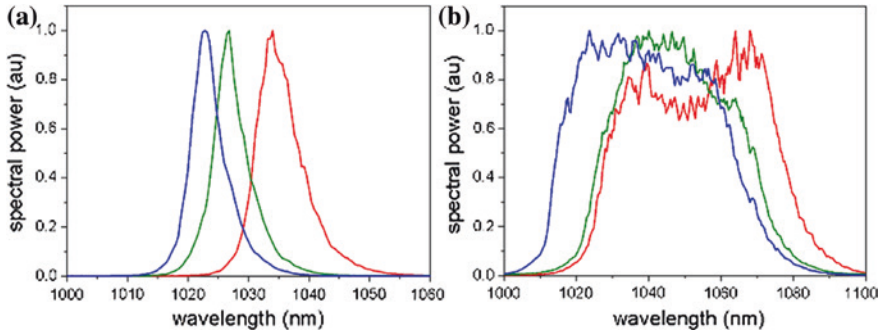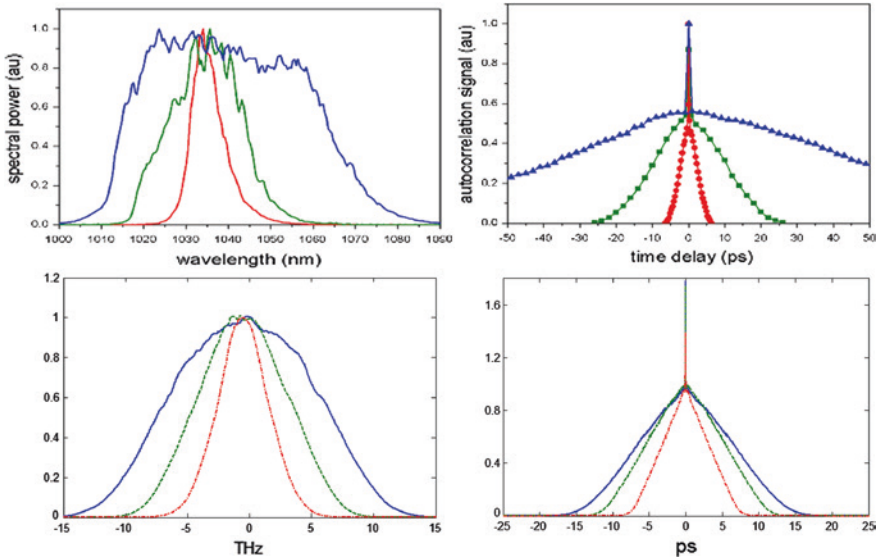
Fig. 3.22 Optical spectra of the measured pulses for different positions of the iris with 1 mm (**a**) and 3 mm (**b**) widths

pulse emission state [41–43, 46]. We observed, however, self-starting noise-like laser operation for a relatively large range of pumping powers. The output powers of noise-like pulses can be varied from <0.1 to >1.6 W (see Fig. 3.21b).

We attribute this improved stability to the laser design where nonlinear polarization evolution is accompanied by self-amplitude modulation induced by spectral filter. The role of negative group velocity dispersion (GVD) induced by gratings pair is also important. In our experiments, this term was set to -0.11 ps^2. According to our estimation, that value is smaller than the total net positive GVD due to the fiber (~0.15 ps^2). Finally, the observed maximal pulse energy at ~13 W pumping power reaches 45 nJ. After increasing pumping power higher than 14 W, one of the fiber couplers was damaged.

In the experiments, we found that by translating the iris transversely across the laser axis, it is possible to modulate the central wavelength of generated pulses. Figure 3.22 demonstrates such results for both narrowband (left) and broadband (right) noise-like pulses. The tuning range for both cases reaches 12 nm. That could be important for some applications. For example, in the case of further amplification of generated pulses by fiber amplifiers, it is necessary to match the bandwidth of oscillator with the gain spectrum of amplifier.

We also found that the diameter of the iris determining filter bandwidth also affects (see Fig. 3.23) the output spectral bandwidth (left) and duration (right) of generated noise-like pulses. In order to understand NLP formation, we simulate the buildup dynamics of our laser cavity by recognizing it as consisting of several connected fiber components. Pulse propagation in each fiber section was described by the corresponding nonlinear Schrodinger coupled-mode equations [see (3.6)]. Dispersive delay line was modeled by introducing a negative GVD of ~0.02 ps^2. High-order dispersion terms were neglected. Wave plates and the polarization beam splitter (PBS) in the cavity were represented by their equivalent Jones matrices in the calculation. For modeling of propagation through each fiber section, we employed the split-step Fourier method [20]. Assuming a thermal Gaussian noise as a source of oscillations, we found the conditions where repeated noise-like

Fig. 3.23 Measured (*top*) and simulated (*bottom*) optical spectra (*left*) and autocorrelation traces (*right*) of output pulses for different (1, 2, and 3 mm) widths of the iris
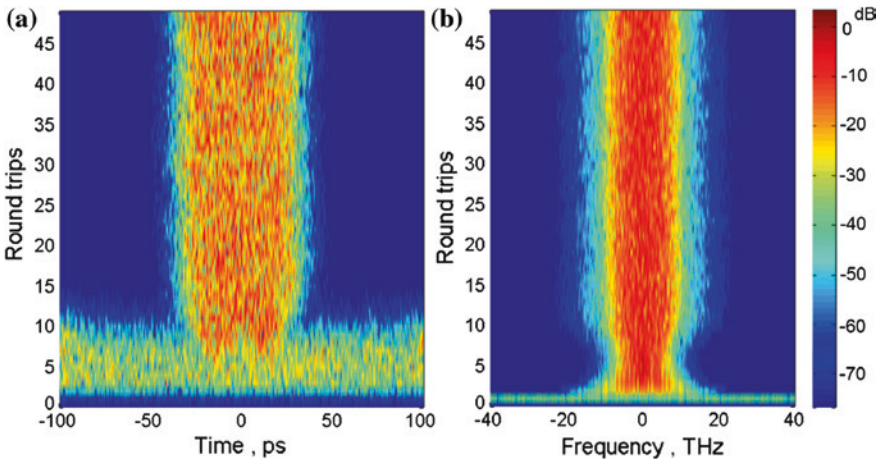
Fig. 3.24 Building up dynamics in time (**a**) and spectral (**b**) domains of a fiber ring oscillator generating NLPs

pulses begin to circulate in the laser cavity after just a few round-trips (see Fig. 3.24). It is significant that all nonlinear terms (self-phase modulation, cross-phase modulation, four-wave mixing, etc.) in (3.6) contribute to NLP creation.

The simulation results for the steady state are in good agreement with experimental observations. The estimated iris filter bandwidth, corresponded iris diameter, output bandwidths and bunch duration are listed in Table 3.3.

Table 3.3 The summary of measured and simulated results for NLPs

Iris diameter (mm)	Iris band-width (THz)	Measured output band-width (THz)	Calculated output band-width (THz)	Measured autocorrela-tion trace half-width (ps)	Calculated autocorrela-tion trace half-width (ps)
1	5	2.1	5	5	7
2	10	4.2	9	20	12
3	20	13.4	15	90	20

We noted that larger output bandwidth corresponds to smaller duration of wave-forms. This is in agreement with observation by previous workers [45]. The dura-tions of wave packets in our case are, however, an order of magnitude shorter than those reported in [45]. Tuning the 3-dB wavelength bandwidth of the NLP laser from 7.6 to 48.2 nm, we were able to vary the duration of NLPs from 90 to 5 ps.

In summary, by using cladding-pumped Yb-doped active fibers and high-power multimode laser diodes, we demonstrated that a passively mode-locked fiber laser can be tuned to generate noise-like pulses with relatively large energies. To the best of our knowledge, the pulse energy of 45 nJ obtained in this work is the high-est for noise-like pulses generated in fiber oscillators reported to the date. The achieved energy is only limited by damage threshold of available fiber couplers. We also found simple method to control temporal and spectral characteristics of noise-like pulses in a large range.

3.2.7 Supercontinuum Generation by the Noise-Like Pulsed YDF Laser

Supercontinuum (SC) light sources are widely employed in optical communica-tion systems, as wavelength tunable sources, gas sensing, and optical metrology. SC generation using photonic crystal fibers (PCF) or microstructured fibers [56], which provide higher nonlinearity and allow one to blue-shift the zero-disper-sion wavelength (ZDW), is quite popular. PCF-based supercontinuum sources can be pumped by efficient powerful light sources at ~800 nm and ~1 µm. However, PCFs are still expensive and not widely available.

Standard single-mode fibers (SMF) for optical communication, on the other hand, are inexpensive and easy to integrate. Compared to PCFs for generation of SC, which normally feature a non-circular symmetry, light propagated through SMF usually exhibits much better spatial beam profile. On the other hand, SC gen-eration in SMFs operating in the normal dispersion regime is not so efficient. It requires much more pulse energy to excite SC compared to the anomalous regime. Also, the SC spectrum so generated exhibits very strong oscillations [57].

Recently, SC generation was reported in a piece of standard fiber (SMF-28) using as the pump a train of NLPs at the central wavelength of 1.5 µm [54]. To excite a flat broadband SC, the energy threshold was as low as ~12 nJ.
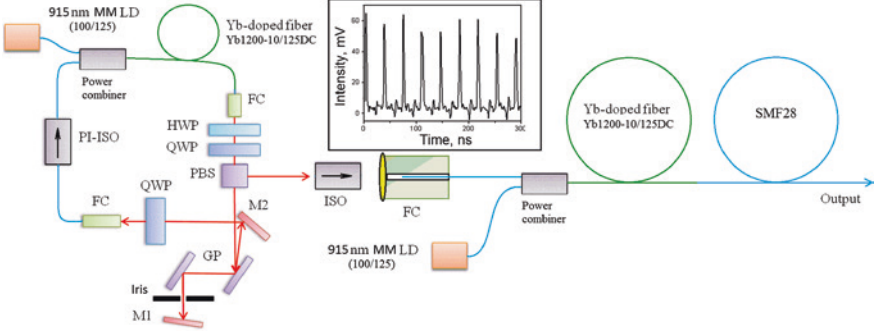
Fig. 3.25 Schematic of the experimental setup: *FC* fiber coupler; *HWP* half-wave plate; *QWP* quarter-wave plate, *GP* grating pair; *PI-ISO* polarization-insensitive isolator; *ISO* Faraday isolator; *M*1 and *M*2 mirrors; *MM LD* multi-mode laser diodes

In the previous section, we demonstrated that a dispersion-mapped Yb-doped fiber laser based on the ring cavity design can generate noise-like pulses with energies as high as ~45 nJ and controllable characteristics at ~1 µm wavelength. The use of negative dispersion delay line and the spatial spectral filter were found to be important for such high-power noise-like operation (see Fig. 3.25). In the NLP regime and pumped at ~10 W, the oscillator irradiates typically a pulse train (see inset at Fig. 3.25) with repetition rate of ~31.5 MHz, average power of ~800 mW and average noise-like bunch duration of ~35 ps.

The iris in the cavity was used to tune the center wavelength from ~1,030 to ~1,070 nm with a bandwidth of ~11 nm (FWHM) [37]. These noise-like pulses were then boosted up to ~3 W in a single 2.3 m-length Yb-doped amplifier stage and used as a pump to excite the SC. A spool of 100 m length of standard SMF (SMF28, POFC, Taiwan) was directly spliced to the output fiber end of the amplifier.

We studied theoretically SC generation in a standard SMF by pumping with either NLP or mode-locked Gaussian pulses of similar pulse energy. The results are calculated by solving the general nonlinear Schrödinger equation in the frequency domain [58]

$$\frac{\partial A'(z,\omega)}{\partial z} = i\frac{\gamma\omega}{\omega_0}\exp\{-L(\omega)z\}F\left\{A(z,T)\int_{-\infty}^{\infty}R(T')\big|A(z,T-T')\big|^2dT'\right\},$$

(3.7)

where A and A' represent the electric field envelopes [58], F{} denotes the Fourier transform, R(t) is the Raman response function [20]

$$R(t) = (1-f_R)\delta(t) + f_R\frac{\tau_1^2+\tau_2^2}{\tau_1\tau_2^2}\exp\left(-\frac{t}{\tau_2}\right)\sin\left(-\frac{t}{\tau_1}\right)\Theta(t),$$

(3.8)

where $f_R = 0.18$ is the fractional contribution of the delayed Raman response; $\tau_1 = 12.2$ fs, and $\tau_2 = 32$ fs. $\Theta(t)$ is the Heaviside step function and $\delta(t)$ is the Dirac delta function. In (3.7), $L(\omega)$ is the linear operator representing dispersion and absorption behaviors of the SMF, given by $L(\omega) = i(\beta(\omega) - \beta(\omega_0) - \beta_1(\omega_0)(\omega - \omega_0)) - \alpha(\omega)/2$. GVD and third-order dispersion (TOD) were assumed to be 0.02 ps^2/m and 25×10^{-6} ps^3/m, typical for SMF28. The non-linear coefficient γ was assumed to be 0.0025 (W m)$^{-1}$. Absorption in fiber was neglected. This approach allows us to treat (3.7) as an ordinary differential equation (ODE) and to use powerful numerical methods, e.g., the 4th order Runge-Kutta method, to solve it. The simulation results for three different types of pulses with pulse energy of 200 nJ each and propagating through 50 m of SMF are presented in Fig. 3.26.

Examining Fig. 3.26, we find that SC evolution in the case of NLP pumping is different from those of mode-locked picosecond or femtosecond Gaussian pulses. It is interesting to note that NLPs, in comparison to mode-locked Gaussian pulses of similar waveform duration (~40 ps), exhibit similar broadening in the time domain after propagation [see Fig. 3.26b and d]. On the other hand, NLPs can generate very broad SC covering the spectral range from 1,030 to 1,700 nm [see Fig. 3.26a and c]. Note that picosecond Gaussian pulses (~40 ps) can only generate three clear Raman peaks in its spectrum (Fig. 3.26c). As for the shorter mode-locked Gaussian pump pulse (200 fs), it can also generate SC from 830 to 1,500 nm (Fig. 3.26e) but the peak pump power needed is 2 orders of magnitude higher than the corresponding NLP of similar pulse energy (~200 nJ). Also, 200 fs-wide Gaussian pump pulses excite SC in first tens of centimeters of the SMF (see inset in Fig. 3.26). Then, its spectrum does not change (see Fig. 3.26e). The evolution of NLP-excited SC takes longer distance in the fiber. Moreover, the spectral broadening occurs mainly in the longer-wavelength (relative to the pump wavelength) region. Recently, it was theoretically predicted that Raman-induced spectral shift, which may happen even in the normal dispersion region is responsible for such an asymmetry [59]. Because of the relative narrow band of the NLPs, this could not be the most effective process for SC generation. The distinctive Raman orders in Fig. 3.26c for mode-locked pulses suggested that multiple Raman processes, i.e., cascaded Raman scattering could have happened for NLP pumped SMF. Therefore, we have tentatively attributed our calculated behavior of the broadband SC emission to Raman amplification of noise in the SMF [56]. The smooth SC spectrum in the case of NLP pumping can be explained by broadband pumping [60], which is a feature of NLP [50].

The spectra of the SC output for different values of average power at the fiber input are shown in Fig. 3.27a (dotted lines). The corresponding simulated SC spectra are plotted as solid lines in Fig. 3.27a. The characteristic asymmetrical spectra hinted that the broadband emission is due to Raman amplification of NLPs [50]. The pulse energy threshold (~43 nJ) to achieve significant spectral broadening, which corresponds to ~1 W of average pump power, is ~4 times larger than that found in the case of work in the anomalous dispersion regime [54]. On the other hand, compared to other reports of SC generation pumped
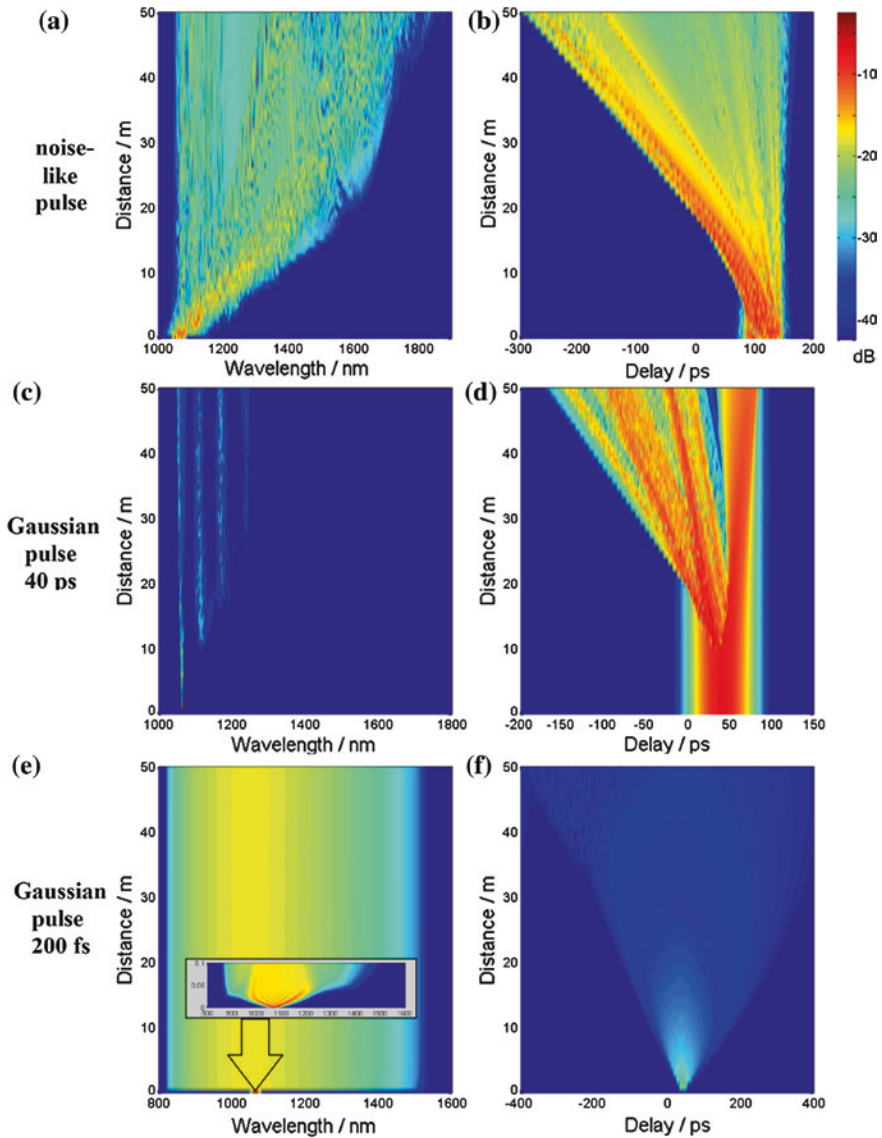
Fig. 3.26 Calculated SC evolution in spectral (**a, c, e**) and time (**b, d, f**) domains for different pump pulses: noise-like pulse (**a, b**), 40 ps-wide mode-locked Gaussian pulses (**c, d**), and 200 fs-wide mode-locked Gaussian pulses (**e, f**)

in the normal-dispersion regime [57, 60–62], the measured threshold is from 1 to 3 orders of magnitudes lower. The measured spectra generated by cascaded Raman scattering is quite uniform, in particular for the 1,050–1,250 nm region. Also, as it can be seen from Fig. 3.27a that the simulated SC spectra matched
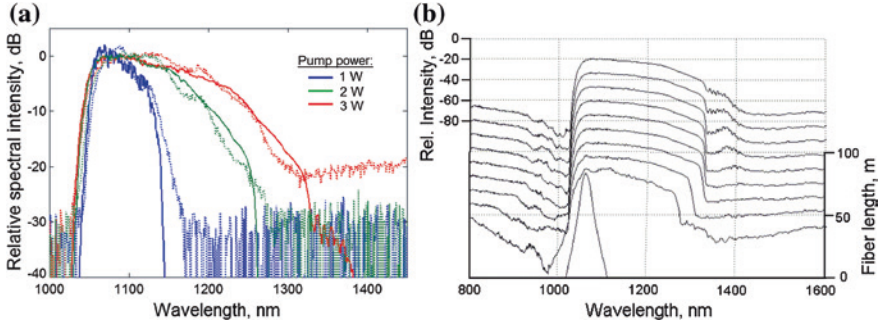
Fig. 3.27 **a** Experimental (*dotted*) and simulated (*solid*) SC spectra generated in 100 m of SMF by pumping with different average NLP input powers (1, 2 and 3 W); **b** simulated spectral evolution of 3 W average power NLP propagating through 100 m of SMF

with experimentally measured ones quite well. The discrepancy is only observed when the generated components approach ZDW. We think that is because of limited number of dispersion terms used for the simulation (only up to 3rd order). It is well known that near the ZDW, higher-order dispersion terms become much more important [20].

Figure 3.27b shows the simulated spectral evolution of NLPs propagating through 100 m of SMF. The average power of the NLP at the input of the SMF is assumed to be 3 W. It can be seen that even after 50 m of SMF, the evolution of SC spectrum is not finished yet. Here underlies some unique features of SC generation by NLPs. First of all, they are broadband just like mode-locked femtosecond pulses. Secondly, they can propagate for much longer distance without distortion and breakup just like mode-locked picosecond pulses. Yet, NLPs contribute new spectral components as they propagate along the SMF.

In summary, we have successfully demonstrated broadband SC generation by noise-like pulses propagating in a piece of 100 m-long standard single-mode fiber operating in the normal dispersion regime. A low energy threshold (43 nJ) and flat SC spectrum over the wavelength range of 1,050–1,250 nm were achieved. Theoretical simulations based on the Schrodinger coupled-mode equations and the general nonlinear Schrodinger equation indicate that the possible physical mechanism of SC generation by this approach is due to cascaded Raman scattering and Kerr effect in the SMF. The Raman effect is responsible for significant spectral broadening the longer wavelength regions whereas the Kerr effect results in smoothing of SC generated spectrum pumped by NLPs.

We believe the achieved low energy threshold and flat SC spectrum are caused by special properties of NLP (broadband spectral range and ability to propagate over a long distance). This new SC light source exhibit attractive characteristics that are potentially competitive to those of the currently used technologies including PCF-based approaches.

3.2.8 Nonlinear Conversion of Picosecond Bursts from Yb-Doped Fiber Laser Amplifiers

Nowadays, UV lasers with the central wavelength at 266 nm are widely used in the fields of medical surgery, chemistry, photolithography, and material sciences. For example, UV light source provide higher resolution and better alignment control in photolithography. Also, the semiconductor industry requires optical inspection tools using lasers with shorter and shorter wavelengths. Because of the continuous reduction in feature size, such sources are essential in order to reach the necessary imaging resolution for wafer inspection [63].

UV laser sources are also popular for scribing and cutting of sapphire and GaN [63]. LED manufacturers increasingly employed either the Q-switched (Nd:YAG or Yb-doped fiber) lasers or cutting tools with diamond blades for wafer scribing. By using the Q-switched laser, the precision of scribing is smaller than 100 μm. This is much better than that achieved by using the diamond blade for scribing. The peak power of the high-repetition-rate Q-switched Nd:YAG or Yb-doped fiber laser, however, is typically not high enough to reach the ablation threshold of many materials. To get better performance in material processing, high pulse energy and shorter wavelength laser sources are desirable.

Recently, laser ablation of metals using bursts of picosecond pulses has been investigated [64–67]. Compared with nanosecond single pulses, there are some benefits for material micromachining in terms of material removal efficiency and the surface quality by using bursts of picosecond pulses. Most of ultrafast laser systems have pulse trains with pulses that are equally spaced in time. There are much interests in lasers that generated a burst of limited number of short pulses. One of the reasons why burst pulses are advantageous for material ablation is that they can keep thermal effect minimized. Thermal effect always depends on the average power irradiated but ablation depends on the peak power. By controlling the repetition rate of the burst, one can easily reduce the unwanted thermal effect. On the other hand, highly repetitive pulses with high pulse energy within the burst not only can enhance the efficiency of material ablation but also improve the efficiency of frequency conversions.

To date, burst-pulse lasers are almost always based on solid-state laser systems. In this work, we constructed Yb-doped fiber based laser amplifier systems that can generate bursts of high-repetition rate picosecond pulses. The energy stored in the gain fiber can be extracted efficiently. We also found the improvement of frequency doubling and frequency quadrupling efficiencies by using LBO and BBO nonlinear crystals respectively using such burst pulses.

Our theoretical analysis is based on our previous work [32] and summarized in Sect. 3.2.1. The small-signal gain G_0 and the saturation energy E_{sat} for the active optical fiber can be determined accordingly. Extending similar works
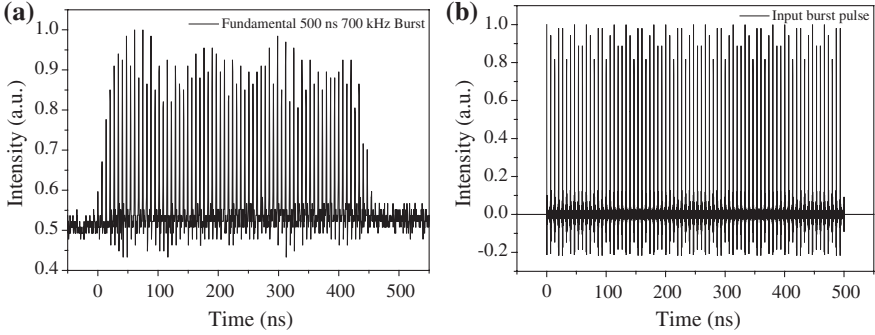
Fig. 3.28 Experimental measurement (**a**) and simulated data (**b**) of input burst pulse with burst duration 500 ns and 700 kHz repetition rate within 10 ps pulse duration and 150 MHz repetition rate

on nanosecond burst pulses, [68–70] the output power P_0 due to amplification of the picosecond burst pulses with energies of $E_i(t)$ can be calculated using the following:

$$P_0(t) = \frac{P_i(t)}{1 - (1 - 1/G_0)e^{(-E_i(t)/E_{sat})}} \tag{3.9}$$

where

$$E_i(t) = \int_{-\infty}^{t} P_i(t')dt' \tag{3.10}$$

The energy $E_i(t)$ of the input picosecond burst can be calculated by integration of input burst in time from 0 to the current time t. From our previous experiment [28], we estimated that the saturation energy of the YDF, $E_{sat} \sim 36.7\ \mu J$. The small signal gain is about 30 dB. Assuming rectangular shape for the input burst, the The experimentally measured and simulated input burst pulses are shown in Fig. 3.28a and b, respectively. In the simulation, we assume 500 ns-wide burst at a repetition rate 700 kHz. Within each burst, there are 10 ps-wide Gaussian pulse at a repetition rate of 150 MHz. These are in accordance with our experimental conditions.

Figure 3.29a and b, on the other hand, show the experimentally measured and theoretically simulated amplified bursts. They indicate a dynamically saturated behavior of fiber amplifier. Compared Figs. 3.28 and 3.29 it can be seen that initially quasi-rectangular envelope input bursts are transferred to exponentially-modulated ones on the amplifier output. That behavior is similar to the case of ns-pulse amplification [68].

Assuming the fundamental beam from the amplified YDF output is not depleted, the intensity of the second-harmonic signal generated in the plane wave approximation is given by

$$I_{2\omega}(z) = 2Z\kappa^2 I_\omega^2(0)z^2 \sin c^2(\Delta kz/2), \tag{3.11}$$
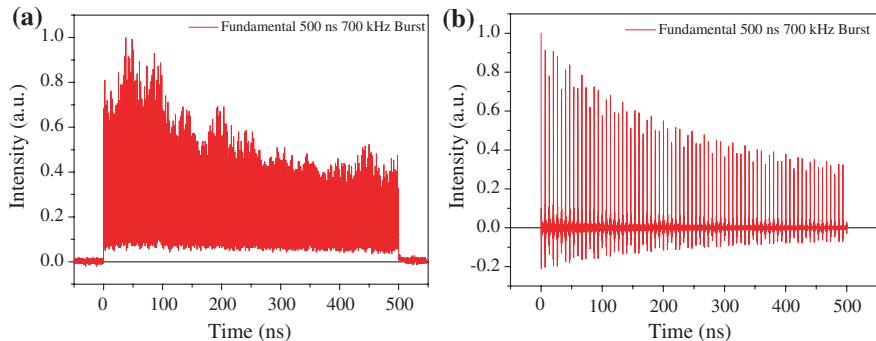
Fig. 3.29 Experimental measurement (**a**) and simulated data (**b**) of output burst pulse train after amplification
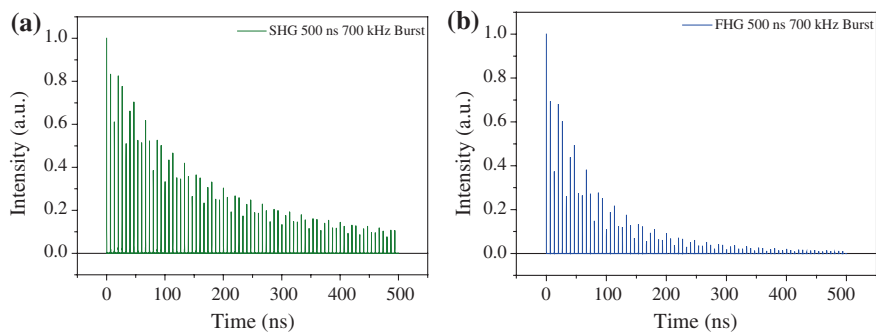

Fig. 3.30 Theoretically simulated results for frequency-doubled (**a**) and quadrupled (**b**) pulse bursts from the MOFA

where $Z = (\mu_0/\varepsilon_0)^{1/2}/n$ is the impedance of the crystal, $\kappa = d_{eff}\, \omega/c_0\, n$ is the coupling coefficient, Δk is the wave vector mismatch and z is the crystal length. The intensity of fourth-harmonic signal can be represented in a similar way. Figure 3.30 shows the simulated pulse trains after frequency doubling (a) and quadrupling (b) of the fundamental pulse burst (see Fig. 2.29b). It can be seen that the shapes of doubled and quadrupled pulse burst become more and more asymmetrical.

We then estimate the nonlinear conversion efficiency for SHG by the pulse burst by integrating the converted SHG within the burst:

$$\eta = \frac{\int_0^\tau P_{2\omega}(z,t)dt}{\int\limits_0^\tau P_\omega(z,t)dt} = \frac{\int_0^\tau \frac{2Z\kappa^2 P_i^2(0,t)z^2\ \sin\ c^2(\Delta kz/2)}{A}dt}{\int\limits_0^\tau \frac{P_i(t)}{1-(1-1/G_0)e^{(-E_i(t)/E_{sat})}}dt}, \tag{3.12}$$

where τ is the period of the burst and A is the effective area of the beam on the nonlinear crystal. Equation (3.12) predicts a conversion efficiency η of about
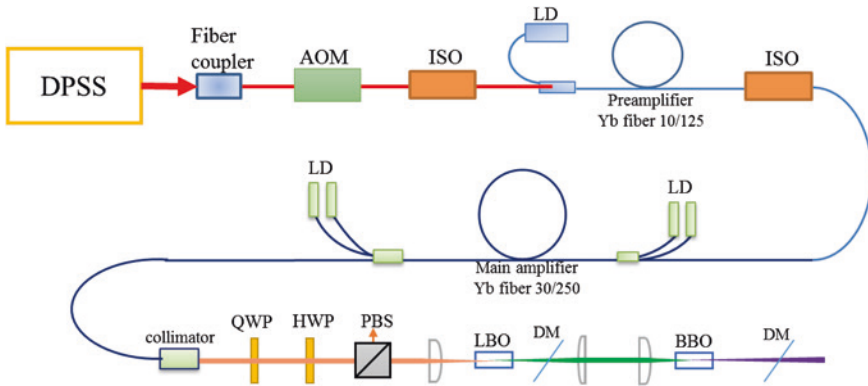
Fig. 3.31 Schematic drawing of the MOFA system and frequency conversion. *AOM* acousto-optic modulation. *ISO* isolator; *LD* laser diode; *QWP* quarter-wave plate. *HWP* half-wave plate. *PBS* polarization beam splitter. *DM* dichroic mirror

17.6 % for the pulse burst versus 8 % for the CW pulse train at 150 MHz. Frequency quadrupled output of the pulse burst can similarly be simulated. The experimental setup is shown schematically in Fig. 3.31.

The MOFA has been described in the previous section. LBO and BBO crystals were used for frequency doubling and quadrupling of the MOFA output. Since non-PM fibers were used, we realized the desired polarization states with appropriate wave plates and polarizing beam splitters. An acousto-optic modulator (AOM) was used to create the desired pulse bursts and control their repetition rate.

To enhance the frequency conversion efficiency, higher peak power from the amplifier output is desirable. For the system described in [25], the output peak power is limited by the pumping power. To enhance the peak power without further pumping, we take advantage of dynamically saturated gain of the fiber amplifier. That is, the front part of pulse burst would experience much larger gain than the tail part of the burst.

We plotted the average output power of the MOFA as a function of pumping power in Fig. 3.32a for the case of regular pulse train (without AOM) and for the case of pulse burst (with AOM). It should be mentioned that the only the spectral output near 1,064 nm was taken into account. From Fig. 3.32a, it is apparent that the output signal power (wavelength at 1,064-nm) become saturated when the pulse burst was amplified at relatively high pumping power (larger than 50 W). Figure 3.32b indicates that the SPM and SRS became significant at these high pumping powers. Thus saturation of the amplifier output is attributed to the presence of these nonlinear effects.

In order to optimize the amplifier performance, we need to prevent the amplified pulse burst from reaching thresholds of these nonlinear effects. One possible way is to reduce the fiber length [20]. The fiber lengths for the preamplifier and the main-amplifier were reduced to 3 and 3.5-m long, respectively. Figure 3.33a
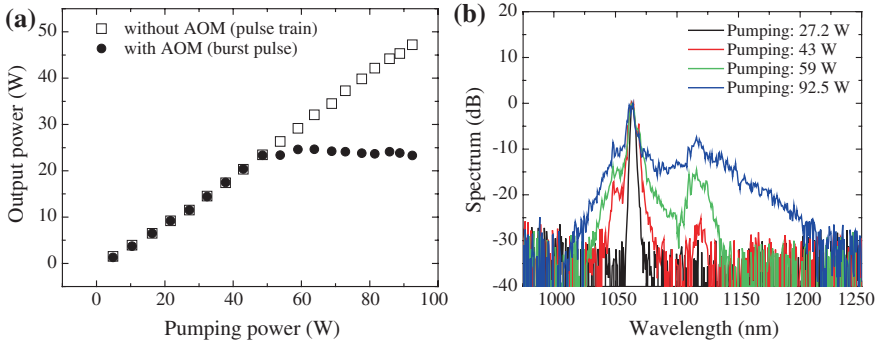
Fig. 3.32 **a** Output power (in a *narrow band* around 1,064 nm) as a function of pumping power with pulse train and burst pulse; **b** Optical spectrum of the burst pulse output
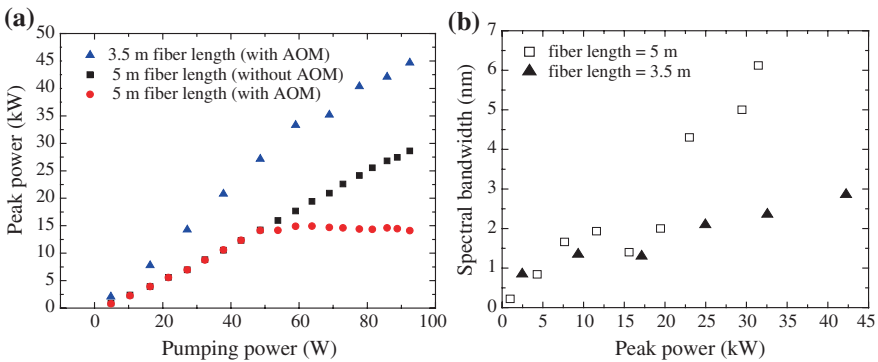

Fig. 3.33 **a** Output peak power as a function of pumping power; **b** the spectral bandwidth as a function of peak power of the 1,064 nm pulse

illustrates that the output peak power of the 3.5-m long fiber length in main-amplifier with using AOM is significantly higher than in the other cases. This is advantageous for applications such as frequency conversion.

In Fig. 3.33b, we show the spectral bandwidths of the burst-mode MOFA as a function of the peak powers for fiber lengths of 5 and 3.5 m in the main amplifier. The bandwidth for the MOFA with shortened fiber can be controlled to ~3 nm at the highest pumping power studied. This is suitable for frequency doubling. The pulse width of the amplified burst was measured by a second-harmonic intensity autocorrelator. The typical second-harmonic intensity autocorrelation trace and corresponding optical spectrum of the burst pulse are shown in Fig. 3.34. The autocorrelation trace is best fit by a double-exponential with FWHM of the pulse intensity profile ~18 ps.

For SHG, we focused the burst-mode MOFA output to a waist size of ~60 μm in the center of a critically phase-matched lithium triborate (LBO) nonlinear crystal. The LBO crystal was 10-mm-long ($\theta = 90°$, $\phi = 11.2°$) and operated at room
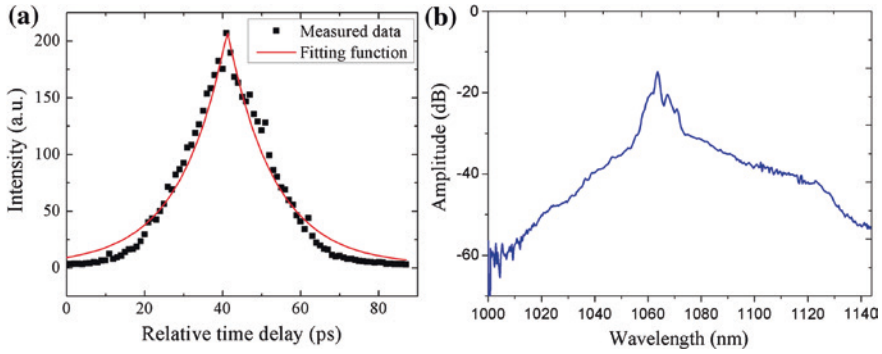
Fig. 3.34 The autocorrelation trace (**a**) and corresponded optical spectrum (**b**) of burst pulse on the MOFA output at ~80 W pump power
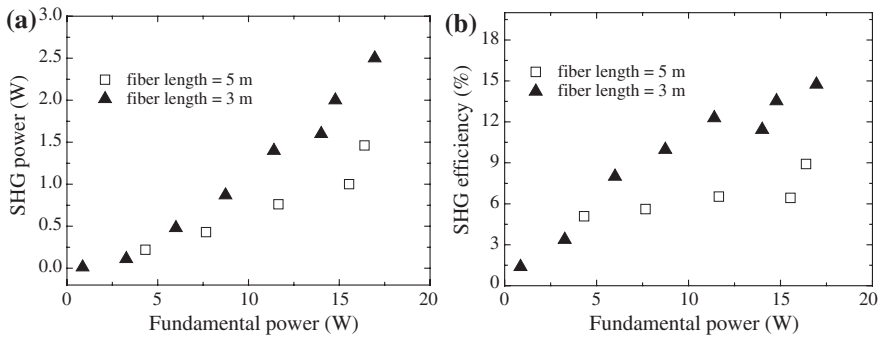
Fig. 3.35 The dependence on fundamental power of **a** average second-harmonic power and **b** efficiency generated by the burst-mode MOFA with two different fiber length for the main amplifier

temperature. After the LBO crystal, a dichroic mirror (DM) is employed to remove the unconverted fundamental light. Lenses were installed to reimage the second-harmonic beam frequency quadrupling.

Figure 3.35 shows the second-harmonic signal generated by the burst-mode MOFA with two different fiber length for the main amplifier. The results show that the output power for MOFA with 3.5-m long Yb-doped fiber is larger than that by the 5-m long Yb-doped fiber in the main-amplifier stage. This is due to the higher fundamental peak power (Fig. 3.33a) and the smaller spectral width (Fig. 3.32b) output generated by the shorter active fiber. Both of these characteristics contribute to the higher conversion efficiency of SHG process (Fig. 3.34b). The 10-mm LBO crystal is expected to have spectral bandwidth acceptance for phase matching of around 3 nm. This matched the spectral bandwidth of the fundamental output from the MOFA system with the shorter active fiber, as can be seen from Fig. 3.32b.
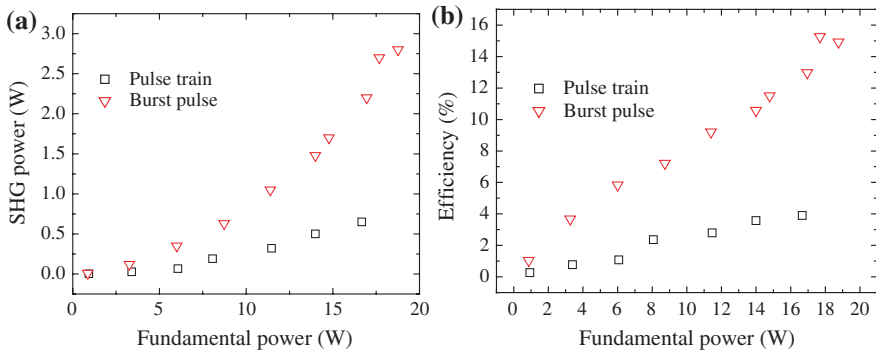
Fig. 3.36 SHG Experimentally measured **a** SHG output power and **b** conversion efficiency of the MOFA as a function of fundamental power. Data for the regular pulse train and burst pulse cases, respectively

We have compared performance of SHG by the regular pulse train output and burst-mode MOFA using the 3.5-m long Yb-doped fiber in the main-amplifier stage. The results are presented in Fig. 3.36. It is obviously to see that the burst pulse have better results than the regular pulse train. The main reason is not only the burst pulse provides the higher peak power, but also the lower thermal influence on crystal when beam passing through LBO. That is caused by lower average fundamental power applied for nonlinear crystal. So, the temperature stabilization is more stable than in the case of regular pulses. The results show that we can obtain ~3 W of SHG power in the burst pulse condition.

We also report fourth harmonic generation (FHG) of our YDF MOFA system. The nonlinear crystal for generation of 266-nm UV light is a beta-barium borate (BBO) crystal, 5-mm-long and cut for type I critical phase matching ($\theta = 47°$, $\phi = 0°$) and operated at room temperature. The second DM installed after the BBO crystal serves to remove the unconverted green light.

Because the efficiency of FHG in the case of regular pulse train is quite low (~1–2 % at maximum), we only present results for the burst-mode of the MOFA. At an average second harmonic input power of 0.5–2.5 W, the typical power of fourth harmonic beam is 20–200 mW. The efficiency of frequency doubling from 532 nm beam is 2–8 % (see Fig. 3.37a). Figure 3.37b summarized the pulse energy and efficiency for generated second and fourth harmonic as a function the fundamental pulse energy. From the figures, we can see that peak powers in excess of 6.7 kW for the second harmonic (532-nm) and 0.6 kW for the fourth harmonic (266-nm) of the MOFA in burst-mode were generated.

In summary, we present an experimental and theoretical study of the generation of picosecond bursts by an Yb-doped fiber MOFA system, which was used to generate 3 W of green and 200 mW of UV light with the conversion efficiencies are 16 and 8 %, respectively. The enhancement of conversion efficiency by the
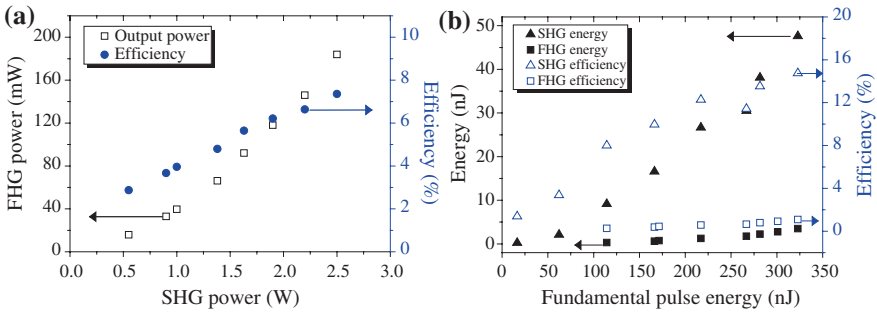
Fig. 3.37 a Performance of fourth harmonic generation; **b** pulse energies and efficiencies of SHG, FHG of the output of the dual-stage MOFA

pulse burst compared with regular pulses was analyzed and attributed to dynamically saturated gain of the pump-power-limited fiber amplifier. The length and output power of Yb-doped fiber were optimized to suppress stimulated Raman scattering (SRS) and self-phase modulation (SPM). The ultimate fiber laser system generates a peak power of fundamental higher than 45 kW and burst pulse energy of 350 nJ. Its harmonics have the peak powers of 6.7 kW (532 nm) and 0.6 kW (266 nm).

3.3 Conclusions

In this chapter, we first considered practical aspects in design and construction of relatively high-average-power picosecond Yb-doped fiber laser systems. Employing a highly stable diode-pumped solid-state laser as the seed source together with proper design of the fiber amplifiers, we were able to achieve an average output power of ~60 W with 73 W pumping using just 2 amplifier stages based on regular non-PM Yb-doped fiber. Applying modulation technique to generate pulse bursts at 700 kHz allowed us to optimize dynamically saturated amplifier and extract higher energies from the MOFA. This was used to improve the nonlinear conversion efficiency in the cases of second (16 % vs. 4 %) and fourth (8 % vs. 2 %) harmonic generation compared to regular pulse trains at ~250 MHz.

   We also described mode-locking techniques of fiber-based oscillators based on ring type cavities with NPE port. Our simulation results based on coupled nonlinear Schrödinger equations showed the possibility to generate either regular mode-locked pulse trains or noise-like pulses in such oscillators. Novel scheme of supercontinuum generation by noise-like pulses in normally dispersive single-mode fibers was demonstrated. The SC exhibits low threshold (43 nJ) and flat spectrum over the wavelength range of 1,050–1,250 nm.

References

1. F. Röser, D. Schimpf, O. Schmidt, B. Ortaç, K. Rademaker, J. Limpert, A. Tünnermann, 90 W average power 100 μJ energy femtosecond fiber chirped-pulse amplification system. Opt. Lett. **32**(15), 2230–2232 (2007). doi:10.1364/OL.32.002230

2. O. Schmidt, J. Rothhardt, F. Röser, S. Linke, T. Schreiber, K. Rademaker, J. Limpert, S. Ermeneux, P. Yvernault, F. Salin, A. Tünnermann, Millijoule pulse energy Q-switched short-length fiber laser. Opt. Lett. **32**(11), 1551–1553 (2007). doi:10.1364/OL.32.001551

3. G. Smith, K. Kalli, K. Sugden. Advances in femtosecond micromachining and inscription of micro and nano photonic devices, in *Frontiers in Guided Wave Optics and Optoelectronics*, ed. by B. Pal. InTech. doi:10.5772/39542 (2010)

4. R.R. Gattass, E. Mazur, Femtosecond laser micromachining in transparent materials. Nature Photon. **2**(4), 219–225 (2008)

5. M. Mielke, D. Gaudiosi, K. Kim, M. Greenberg, X. Gu, R. Cline, X. Peng, M. Slovick, N. Allen, M. Manning, M. Ferrel, N. Prachayaamorn, S. Sapers, Ultrafast fiber laser platform for advanced materials processing. J. Laser Micro/Nanoeng. **5**(1), 53–58 (2010). doi:10.2961/jlmn.2010.01.0012

6. R. Paschotta, J. Nilsson, A.C. Tropper, D.C. Hanna, Ytterbium-doped fiber amplifiers. IEEE J. Quantum Electron. **33**(7), 1049–1056 (1997). doi:10.1109/3.594865

7. H.M. Pask, R.J. Carman, D.C. Hanna, A.C. Tropper, C.J. Mackechnie, P.R. Barber, J.M. Dawes, Ytterbium-doped silica fiber lasers: versatile sources for the 1–1.2 μm region. Sel. Top. Quantum Electron. **1**(1), 2–13 (1995). doi:10.1109/2944.468377

8. D.J. Richardson, J. Nilsson, W.A. Clarkson, High power fiber lasers: current status and future perspectives. JOSA B **27**(11), B63–B92 (2010). doi:10.1364/JOSAB.27.000B63

9. T. Eidam, S. Hanf, E. Seise, T.V. Andersen, T. Gabler, C. Wirth, T. Schreiber, J. Limpert, A. Tünnermann, Femtosecond fiber CPA system emitting 830 W average output power. Opt. Lett. **35**(2), 94–96 (2010). doi:10.1364/OL.35.000094

10. F. Röser, J. Rothhard, B. Ortac, A. Liem, O. Schmidt, T. Schreiber, J. Limpert, A. Tünnermann, 131 W 220 fs fiber laser system. Opt. Lett. **30**(20), 2754–2756 (2005). doi:10.1364/OL.-30.002754

11. J. Thieme, Fiber laser—new challenges for the materials processing. Laser Tech. J. **4**(3), 58–60 (2007). doi:10.1002/latj.200790168

12. M.E. Fermann, I. Hartl, Fiber laser based hyperspectral sources. Laser Phys. Lett. **6**(1), 11–21 (2009). doi:10.1002/lapl.200810090

13. A. Tuennermann, S. Nolte, J. Limpert, Femtosecond vs. picosecond laser material processing. Laser Tech. J. **7**(1), 34–38 (2010). doi:10.1002/latj.201090006

14. L. Goldberg, J.P. Koplow, R.P. Moeller, D.A.V. Kliner, High-power superfluorescent source with a side-pumped Yb-doped double-cladding fiber. Opt. Lett. **23**(13), 1037–1039 (1998). doi:10.1364/OL.23.001037

15. J. Limpert, T. Clausnitzer, A. Liem, T. Schreiber, H.J. Fuchs, H. Zellmer, E.B. Kley, A. Tünnermann, High-average-power femtosecond fiber chirped-pulse amplification system. Opt. Lett. **28**(20), 1984–1986 (2003). doi:10.1364/OL.28.001984

16. J. Yoonchan, J. Nilsson, J.K. Sahu, D.N. Payne, R. Horley, L.M.B. Hickey, P.W. Turner, Power scaling of single-frequency ytterbium-doped fiber master-oscillator power-amplifier sources up to 500 W. Sel. Topics Quantum Electron. **13**(3), 546–551 (2007). doi:10.1109/JSTQE.2007.896639

17. X. Wang, P. Li, H. Yang, T. Jiang, Y. Ma, Z. Fan, G. Niu, J. Yu, A. Wang, Z. Zhang, Microjoule level femtosecond optical pulses with double-cladding fiber-based nonlinear chirped-pulse amplification. Laser Phys. **21**(11), 1941–1944 (2011). doi:10.1134/S1054660X11190315

18. A. Fernández, L. Zhu, A.J. Verhoef, D. Sidorov-Biryukov, A. Pugzlys, A. Galvanauskas, F.Ö. Ilday, A. Baltuška, Pulse fidelity control in a 20-μJ sub-200-fs monolithic Yb-fiber amplifier. Laser Phys. **21**(7), 1329–1335 (2011). doi:10.1134/S1054660X11130111

19. C. Zheng, H.T. Zhang, W.Y. Cheng, M. Liu, P. Yan, M.L. Gong, All-fiber millijoule energy and nanoseconds pulse operation of a high beam quality multi-stage pulse-pumped Yb-doped amplifier cascade. Laser Phys. **22**(3), 605–608 (2012). doi:10.1134/S1054660X12030309

20. G.P. Agrawal, *Nonlinear Fiber Optics* (Academic, San Diego, 2007)

21. R.H. Stolen, Polarization effects in fiber Raman and Brillouin lasers. IEEE J. Quantum Electron. **15**(10), 1157–1160 (1979). doi:10.1109/JQE.1979.1069913

22. F. Krausz, M. Ivanov, Attosecond physics. Rev. Mod. Phys. **81**(1), 163–234 (2009). doi:10.1103/RevModPhys.81.163

23. X. Liu, D. Du, G. Mourou, Laser ablation and micromachining with ultrashort laser pulses. IEEE J. Quantum Electron. **33**(10), 1706–1716 (1997). doi:10.1109/3.631270

24. K. Sugioka, M. Meunier, A. Pique, *Laser Precision Microfabrication* (Springer, Berlin, 2010)

25. A.K. Zaytsev, C.L. Wang, C.H. Lin, C.L. Pan, Robust diode-end-pumped Nd:GdVO4 laser passively mode-locked with saturable output coupler. Laser Phys. **21**(12), 2029–2035 (2011). doi:10.1134/S1054660X11210316

26. A.K. Zaytsev, C.L. Wang, C.H. Lin, Y.J. You, F.H. Tsai, C.L. Pan, Effective pulse recompression after nonlinear spectral broadening in picosecond Yb-doped fiber amplifier. Laser Phys. **22**(2), 447–450 (2012). doi:10.1134/S1054660X12020259

27. A.A.M. Saleh, R.M. Jopson, J.D. Evankow, J. Aspell, Modeling of gain in erbium-doped fiber amplifiers. IEEE Photon. Tech. Lett. **2**(10), 714–717 (1990). doi:10.1109/68.60769

28. C. Barnard, P. Myslinski, J. Chrostowski, M. Kavehrad, Analytical model for rare-earth-doped fiber amplifiers and lasers. IEEE J. Quantum Electron. **30**(8), 1817–1830 (1994). doi:10.1109/3.301646

29. T. Pfeiffer, H. Bulow, Analytical gain equation for erbium-doped fiber amplifiers including mode field profiles and dopant distribution. IEEE Photon. Tech. Lett. **4**(5), 449–451 (1992). doi:10.1109/68.136482

30. J.W. Dawson, M.J. Messerly, R.J. Beach, M.Y. Shverdin, E.A. Stappaerts, A.K. Sridharan, P.H. Pax, J.E. Heebner, C.W. Siders, C.P.J. Barty, Analysis of the scalability of diffraction-limited fiber lasers and amplifiers to high average power. Opt. Express **16**(17), 13240–13266 (2008). doi:10.1364/OE.16.013240

31. M.J.F. Digonnet, *Rare-Earth-Doped Fiber Lasers and Amplifiers* (Marcel Dekker, NY, 2001)

32. Y.-J. You, C.-H. Lin, A. Zaytsev, F.-H. Tsai, C.-L. Wang, C.-L. Pan, Optimal design of a high-power picosecond laser system using a dual-stage ytterbium-doped fibre amplifier. Laser Phys. **23**(7), 075114 (2013). doi:10.1088/1054-660X/23/7/075114

33. M.J. Hekmat, M.M. Dashtabi, S.R. Manavi, E. Hassanpour, R. Massudi, Selection of suitable pump diode laser parameters and their effects on efficiency and optimum length of Yb-doped double clad fiber lasers. Laser Phys. **22**(10), 1581–1585 (2012). doi:10.1134/S1054660-X12100088

34. R.I. Laming, J.E. Townsend, D.N. Payne, F. Meli, G. Grasso, E.J. Tarbox, High-power erbium-doped-fiber amplifiers operating in the saturated regime. IEEE Photon. Tech. Lett. **3**(3), 253–255 (1991). doi:10.1109/68.79772

35. E. Desurvire, Analysis of gain difference between forward- and backward-pumped erbium-doped fiber amplifiers in the saturation regime. IEEE Photon. Tech. Lett. **4**(7), 711–714 (1992). doi:10.1109/68.145247

36. M. Hofer, M.H. Ober, F. Haberl, M.E. Fermann, Characterization of ultrashort pulse formation in passively mode-locked fiber lasers. IEEE J. Quantum Electron. **28**(3), 720–728 (1992). doi:10.1109/3.124997

37. A. Zaytsev, C.-H. Lin, Y.-J. You, C.-C. Chung, C.-L. Wang, C.-L. Pan, Supercontinuum generation by noise-like pulses transmitted through normally dispersive standard single-mode fibers. Opt. Express **21**(13), 16056–16062 (2013). doi:10.1364/OE.21.016056

38. H. Lim, F.Ö. Ilday, F.W. Wise, Generation of 2-nJ pulses from a femtosecond ytterbium fiber laser. Opt. Lett. **28**(8), 660–662 (2003). doi:10.1364/OL.28.000660

39. K. Tamura, E.P. Ippen, H.A. Haus, L.E. Nelson, 77-fs pulse generation from a stretched-pulse mode-locked all-fiberring laser. Opt. Lett. **18**(13), 1080–1082 (1993). doi:10.1364/OL.18.00-1080

40. A.K. Zaytsev, C.H. Lin, Y.J. You, F.H. Tsai, C.L. Wang, C.L. Pan, A controllable noise-like operation regime in a Yb-doped dispersion-mapped fiber ring laser. Laser Phys. Lett. **10**(4), 045104 (2013). doi:10.1364/OE.21.016056

41. F. ÖIlday, J.R. Buckley, H. Lim, F.W. Wise, W.G. Clark, Generation of 50-fs, 5-nJ pulses at 1.03?m from a wave-breaking-free fiber laser. Opt. Lett. **28**(15):1365–1367. (2003) doi:10.1364/OL.28.001365

42. J.R. Buckley, S.W. Clark, F.W. Wise, Generation of ten-cycle pulses from an ytterbium fiber laser with cubic phase compensation. Opt. Lett. **31**(9), 1340–1342 (2006). doi:10.1364/OL.31.001340

43. M.E. Fermann, V.I. Kruglov, B.C. Thomsen, J.M. Dudley, J.D. Harvey, Self-similar propagation and amplification of parabolic pulses in optical fibers. Phys. Rev. Lett. **84**(26), 6010–6013 (2000)

44. A. Chong, J. Buckley, W. Renninger, F. Wise, All-normal-dispersion femtosecond fiber laser. Opt. Express **14**(21), 10095–10100 (2006). doi:10.1364/OE.14.010095

45. O. Pottiez, R. Grajales-Coutiño, B. Ibarra-Escamilla, E.A. Kuzin, J.C. Hernández-García, Adjustable noiselike pulses from a figure-eight fiber laser. Appl. Opt. **50**(25), E24–E31 (2011). doi:10.1364/AO.50.000E24

46. S. Kobtsev, S. Kukarin, S. Smirnov, S. Turitsyn, A. Latkin, Generation of double-scale femto/pico-secondoptical lumps in mode-locked fiber lasers. Opt. Exp. **17**(23), 20707–20713 (2009). doi:10.1364/OE.17.020707

47. Y. An, D. Shen, W. Zhao, J. Long, Characteristics of pulse evolution in mode-locked thulium-doped fiber laser. Opt. Comm. **285**(7), 1949–1953 (2012). doi:10.1016/j.optcom.2011.12.001

48. S.M. Kobtsev, S.V. Smirnov, Fiber lasers mode-locked due to nonlinear polarization evolution: Golden mean of cavity length. Laser Phys. **21**(2), 272–276 (2011). doi:10.1134/S1054660-X11040050

49. L.M. Zhao, D.Y. Tang, J. Wu, X.Q. Fu, S.C. Wen, Noise-like pulse in a gain-guided soliton fiber laser. Opt. Exp. **15**(5), 2145–2150 (2007). doi:10.1364/OE.15.002145

50. M. Horowitz, Y. Barad, Y. Silberberg, Noiselike pulses with a broadband spectrum generated from an erbium-doped fiber laser. Opt. Lett. **22**(11), 799–801 (1997). doi:10.1364/OL.22.000-799

51. M. Horowitz, Y. Silberberg, Control of noiselike pulse generation in erbium-doped fiber lasers. IEEE Photon. Tech. Lett. **10**(10), 1389–1391 (1998). doi:10.1109/68.720270

52. Y. Li, A. Hoskins, F. Schlottau, K.H. Wagner, C. Embry, W.R. Babbitt, Ultrawideband coherent noise lidar range-Doppler imaging and signal processing by use of spatial-spectral holography in inhomogeneously broadened absorbers. Appl. Opt. **45**(25), 6409–6420 (2006). doi:10.1364/AO.45.006409

53. J.C. Hernandez-Garcia, O. Pottiez, J.M. Estudillo-Ayala, Supercontinuum generation in a standard fiber pumped by noise-like pulses from a figure-eight fiber laser. Laser Phys. **22**(1), 221–226 (2012). doi:10.1134/S1054660X1123006X

54. J.C. Hernandez-Garcia, O. Pottiez, J.M. Estudillo-Ayala, R. Rojas-Laguna, Numerical analysis of a broadband spectrum generated in a standard fiber by noise-like pulses from a passively mode-locked fiber laser. Opt. Comm. **285**(7), 1915–1919 (2012). doi:10.1016/j.optcom.2011.12.069

55. L.M. Zhao, D.Y. Tang, Generation of 15-nJ bunched noise-like pulses with 93-nm bandwidth in an erbium-doped fiber ring laser. Appl. Phys. B **83**(4), 553–557 (2006). doi:10.1007/s00340-006-2179-0

56. J.M. Dudley, G. Genty, S. Coen, Supercontinuum generation in photonic crystal fiber. Rev. Mod. Phys. **78**(4), 1135–1184 (2006). doi:10.1103/RevModPhys.78.1135

57. C. Lin, V.T. Nguyen, W.G. French, Wideband near-I.R. continuum (0.7–2.1 μm) generated in low-loss optical fibres. Electron. Lett. **14**(25), 822–823 (1978). doi:10.1049/el:19780556

58. J.M. Dudley, J.R. Taylor, *Supercontinuum generation in optical fibers* (Cambridge University Press, Cambridge, 2010)

59. J. Santhanam, G.P. Agrawal, Raman-induced spectral shifts in optical fibers: general theory based on the moment method. Opt. Comm. **222**(1–6), 413–420 (2003). doi:10.1016/S0030-4018(03)01561-X

60. I. Ilev, H. Kumagai, K. Toyoda, I. Koprinkov, Highly efficient widebandcontinuum generation in a single-modeoptical fiber by powerful broadband laser pumping. Appl. Opt. **35**(15), 2548–2553 (1996). doi:10.1364/AO.35.002548

61. R.S. Watt, C.F. Kaminski, J. Hult, Generation of supercontinuum radiation in conventional single-mode fibre and its application to broadband absorption spectroscopy. Appl. Phys. B **90**(1), 47–53 (2008). doi:10.1007/s00340-007-2812-6

62. H. Chen, Y. Lei, S. Chen, J. Hou, Q. Lu, Experimentally investigate the nonlinear amplifying process of high power picoseconds fiber amplifier. Opt. Laser Tech. **47**, 278–282 (2013). doi:10.1016/j.optlastec.2012.09.010

63. D. Karnakis, E.K. Illy, M.R.H. Knowles, E. Gu, M.D. Dawson, High-throughput scribing for the manufacture of LED components. SPIE 5366 (2004) doi:10.1117/12.531685

64. P. Deladurantaye, A. Cournoyer, Drolet M, Desbiens L, Lemieux D, Briand M, Taillon Y (2011) Material micromachining using bursts of high repetition rate picosecond pulses from a fiber laser source. Proc. SPIE 7914. doi:10.1117/12.875265

65. H. Kalaycioglu, K. Eken, F.Ö. Ilday, Fiber amplification of pulse bursts up to 20 µJ pulse energy at 1 kHz repetition rate. Opt. Lett. **36**(17), 3383–3385 (2011). doi:10.1364/OL.36.003383

66. H. Kalaycioglu, Y.B. Eldeniz, Ö. Akçaalan, S. Yava, K. Gürel, M. Efe, F.Ö. Ilday, 1 mJ pulse bursts from a Yb-doped fiber amplifier. Opt. Lett. **37**(13), 2586–2588 (2012). doi:10.1364/OL.-37.002586

67. Y. Ren, C.W. Cheng, J.K. Chen, Y. Zhang, D.Y. Tzou, Thermal ablation of metal films by femtosecond laser bursts. Int. J. Therm. Sci. **70**, 32–40 (2013). doi:10.1016/j.ijthermalsci.2013.03.003

68. D.N. Schimpf, C. Ruchert, D. Nodop, J. Limpert, A. Tünnermann, F. Salin, Compensation of pulse-distortion in saturated laser amplifiers. Opt. Exp. **16**(22), 17637–17646 (2008). doi:10.1364/OE.16.017637

69. A. Malinowski, K.T. Vu, K.K. Chen, J. Nilsson, Y. Jeong, S. Alam, D. Lin, D.J. Richardson, High power pulsed fiber MOPA system incorporating electro-optic modulator based adaptive pulse shaping. Opt. Express **17**(23), 20927–20937 (2009). doi:10.1364/OE.17.020927

70. A. Agnesi, L. Carrà, P. Dallocchio, F. Pirzio, G. Reali, S. Lodo, G. Piccinno, 50-mJ macropulses at 1,064 nm from a diode-pumped picosecond laser system. Opt. Exp. **19**(21), 20316–20321 (2011). doi:10.1364/OE.19.020316